Production of HONO from NO_2 uptake on illuminated TiO_2 aerosol particles and following the illumination of mixed TiO_2/ammonium nitrate particles. ~~Production of HONO from heterogeneous uptake of NO_2 on illuminated TiO_2 aerosols measured by Photo-Fragmentation Laser Induced Fluorescence.~~

Joanna E. Dyson[1], Graham A. Boustead[1], Lauren T. Fleming[1], Mark Blitz[1, 2], Daniel Stone[1], Stephen R. Arnold[3], Lisa K. Whalley[1, 2], Dwayne E. Heard[1]*

[1] School of Chemistry, University of Leeds, LS2 9JT, UK.

[2] National Centre of Atmospheric Science, University of Leeds, LS2 9JT, UK.

[3] School of Earth and Environment, University of Leeds, LS2 9JT, UK.

*Corresponding Author. Email: D.E.Heard@leeds.ac.uk

Abstract

The rate of production of HONO from illuminated TiO_2 aerosols in the presence of NO_2 was measured using an aerosol flow tube system coupled to a photo-fragmentation laser induced fluorescence detection apparatus. The reactive uptake coefficient of NO_2 to form HONO, $\gamma_{NO_2 \rightarrow HONO}$, was determined for NO_2 mixing ratios in the range $34 - 400$ ppb, with $\gamma_{NO_2 \rightarrow HONO}$ spanning the range $(9.97 \pm 3.52) \times 10^{-6}$ to $(1.26 \pm 0.17) \times 10^{-4}$ at a relative humidity of 15 ± 1 % and for a lamp photon flux of $(1.63 \pm 0.09) \times 10^{16}$ photons cm^{-2} s^{-1} (integrated between 290 and 400 nm), which is similar to midday ambient actinic flux values. $\gamma_{NO_2 \rightarrow HONO}$ increased as a function of NO_2 mixing ratio at low NO_2 before peaking at $(1.26 \pm 0.17) \times 10^{-4}$ at ~51 ppb NO_2 and then sharply decreasing at higher NO_2 mixing ratios, rather than levelling off which would be indicative of surface saturation. The dependence of HONO production on relative humidity was also investigated, with a peak in production of HONO from TiO_2 aerosol surfaces found at ~25 % RH. Possible mechanisms consistent with the observed trends in both the HONO production and reactive uptake coefficient were investigated using a zero-dimensional kinetic box model. The modelling studies supported a mechanism for HONO production on

29 the aerosol surface involving two molecules of NO_2, as well as a surface HONO loss

30 mechanism which is dependent upon NO_2. In a separate experiment, significant production of

31 HONO was observed from illumination of mixed nitrate/TiO_2 aerosols in the absence of NO_2.

32 However, no production of HONO was seen from the illumination of nitrate aerosols alone.

33 The rate of production of HONO observed from mixed nitrate/TiO_2 aerosols was scaled to

34 ambient conditions found at the Cape Verde Atmospheric Observatory (CVAO) in the remote

35 tropical marine boundary layer. The rate of HONO production from aerosol particulate nitrate

36 photolysis containing a photocatalyst was found to be similar to the missing HONO production

37 rate necessary to reproduce observed concentrations of HONO at CVAO. These results provide

38 evidence that particulate nitrate photolysis may have a significant impact on the production of

39 HONO and hence NO_x in the marine boundary layer where mixed aerosols containing nitrate

40 and a photocatalytic species such as TiO_2, as found in dust, are present.

1   Introduction

43 A dominant source of OH radicals in polluted environments is the photolysis of nitrous acid

44 (HONO) (Platt et al., 1980;Winer and Biermann, 1994;Harrison et al., 1996;Alicke et al.,

45 2002;Whalley et al., 2018;Crilley et al., 2019;Lu et al., 2019;Slater et al., 2020;Whalley et al.,

46 2020). During a recent study in Winter in central Beijing, HONO photolysis accounted for over

47 90 % of the primary production of OH averaged over the day (Slater et al., 2020). Oxidation

48 by OH radicals is the dominant removal mechanism for many tropospheric trace gases, such as

49 tropospheric methane, as well as the formation of secondary species, including tropospheric

50 ozone (Levy, 1971), nitric and sulphuric acids which condense to form aerosols, and secondary

51 organic aerosols. Understanding the formation of HONO in highly polluted environments is

52 crucial to fully understand both the concentration and distribution of key atmospheric radical

53 species, as well as secondary products in the gas and aerosol phases associated with climate

54 change and poor air quality.

55 Atmospheric concentrations of HONO range from a few pptv in remote clean environments

56 (Reed et al., 2017) to more than 10 ppb in highly polluted areas such as Beijing (Crilley et al.,

57 2019). The main gas-phase source of HONO in the troposphere is the reaction of nitric oxide

58 (NO) with the OH radical. HONO has also been shown to be directly emitted from vehicles

59 (Kurtenbach et al., 2001;Li et al., 2008), for which the rate of emission is often estimated as a

60 fraction of known NO_x (NO_2+NO) emissions. Many heterogeneous HONO sources have also

been postulated including the conversion of nitric acid (HNO_3) on ground or canopy surfaces (Zhou et al., 2003;George et al., 2005), bacterial production of nitrite on soil surfaces (Su et al., 2011;Oswald et al., 2013) and, more recently, particulate nitrate photolysis, thought to be an important source in marine environments (Ye et al., 2016;Reed et al., 2017;Ye et al., 2017a;Ye et al., 2017b). Rapid cycling of gas-phase nitric acid to gas-phase nitrous acid via particulate nitrate photolysis in the clean marine boundary layer has been observed during the 2013 NOMADSS aircraft measurements campaign over the North Atlantic Ocean (Ye et al., 2016). Ground-based measurements of HONO made at Cape Verde in the tropical Atlantic Ocean (Reed et al., 2017) provided evidence that a mechanism for renoxification in low NO_x areas is required (Reed et al., 2017;Ye et al., 2017a).

Recent model calculations show a missing daytime source of HONO, which is not consistent with known gas-phase production mechanisms, direct emissions or dark heterogeneous formation (e.g. prevalent at night). It has been suggested that this source could be light driven and dependent on NO_2 (Kleffmann, 2007;Michoud et al., 2014;Spataro and Ianniello, 2014;Lee et al., 2016).

It is estimated that between 1604 and 1960 Tg yr^{-1} of dust particles are emitted into the atmosphere (Ginoux et al., 2001). Titanium dioxide (TiO_2) is a photocatalytic compound found in dust particles at mass mixing ratios of between 0.1 and 10 % depending on the location the particles were suspended (Hanisch and Crowley, 2003). When exposed to UV light ($\lambda < 390$ nm) TiO_2 promotes an electron (e_{CB}^-) from the conduction band to the valence band leaving behind a positively charged hole (h_{VB}^+) in the valence band (Chen et al., 2012):

$$TiO_2 + h\nu \rightarrow e_{CB}^- + h_{VB}^+ \qquad\qquad\qquad (R1)$$

which can then lead to both reduction and oxidation reactions of any surface adsorbed gas-phase species such as NO_2 leading to HONO.

In previous studies of the reaction of NO_2 on TiO_2 aerosol surfaces, HONO was observed as a major gas-phase product (Gustafsson et al., 2006;Dupart et al., 2014). Gustafsson *et al.*, (2006) observed a yield of gas-phase HONO of ~ 75 % (for each NO_2 removed), and showed the rate of the photoreaction of NO_2 on pure TiO_2 aerosols depended on relative humidity, emphasising the superhydrophilic nature of TiO_2 surfaces under UV irradiation. Dupart *et al.* (2014) also reported a relative humidity dependence of the uptake of NO_2 onto Arizona Test Dust containing TiO_2 with the main gas-phase products measured being NO and HONO, with a HONO yield of 30 % in experiments with 110 ppb NO_2. Dupart et al. (2014) postulated the

following mechanism of HONO production, which is consistent with the formation of the NO_2^- anion seen in a previous study on TiO_2 surfaces (Nakamura et al., 2000):

$$h_{VB}^+ + H_2O \rightarrow H^+ + OH \tag{R2}$$

$$e_{CB}^- + O_2 \rightarrow O_2^- \tag{R3}$$

$$NO_2 + O_2^- (or\ e_{CB}^-) \rightarrow NO_2^- + O_2 \tag{R4}$$

$$NO_2^- + H^+ \rightarrow HONO \tag{R5}$$

$$NO_2 + OH \rightarrow HNO_3 \tag{R6}$$

In areas with high mineral dust loading, such as desert regions, far from anthropogenic sources, NO_2 concentrations are typically low. However, when dust is transported to urban areas, this source of HONO may become significant. One study reported that TiO_2 composed 0.75-1.58 µg m^{-3} when aerosol loadings were 250-520 µg m^{-3} over the same time period in southeast Beijing, when air had been transported from the Gobi desert (Schleicher et al., 2010).

In this study, the production of HONO on the surface of TiO_2 particles in the presence of NO_2 is investigated as a function of NO_2 mixing ratio, aerosol surface area density and relative humidity using an aerosol flow tube system coupled to a photo-fragmentation laser induced fluorescence detector (Boustead, 2019). The uptake coefficient of NO_2 to generate HONO is then determined, and a mechanistic interpretation of the experimental observations is presented. The production of HONO directly in the absence of NO_2 from the illumination of a mixed sample of nitrate and TiO_2 aerosol is also presented. Using a similar apparatus, previous work had showed that TiO_2 particles produce OH and HO_2 radicals directly under UV illumination (Moon et al., 2019). The atmospheric implications of these results and the role of photo-catalysts for the formation of HONO are also discussed.

2 Method

2.1 Overview of the Experimental Setup

The production of HONO from illuminated aerosol surfaces is studied using an aerosol flow tube system coupled to a photo-fragmentation laser induced fluorescence (PF-LIF) cell which allows the highly sensitive detection of the OH radical formed through photo-fragmentation of HONO into OH and NO followed by Laser-Induced Fluorescence (LIF) detection at low pressure. The experimental setup used in this investigation is described in detail in (Boustead, 2019), as well as similar systems having been used to measure HONO in the field (Liao et al.,

117 2006;Wang et al., 2020),and therefore only a brief description of the setup is given here. A
118 schematic of the experimental setup is shown in Figure 1.
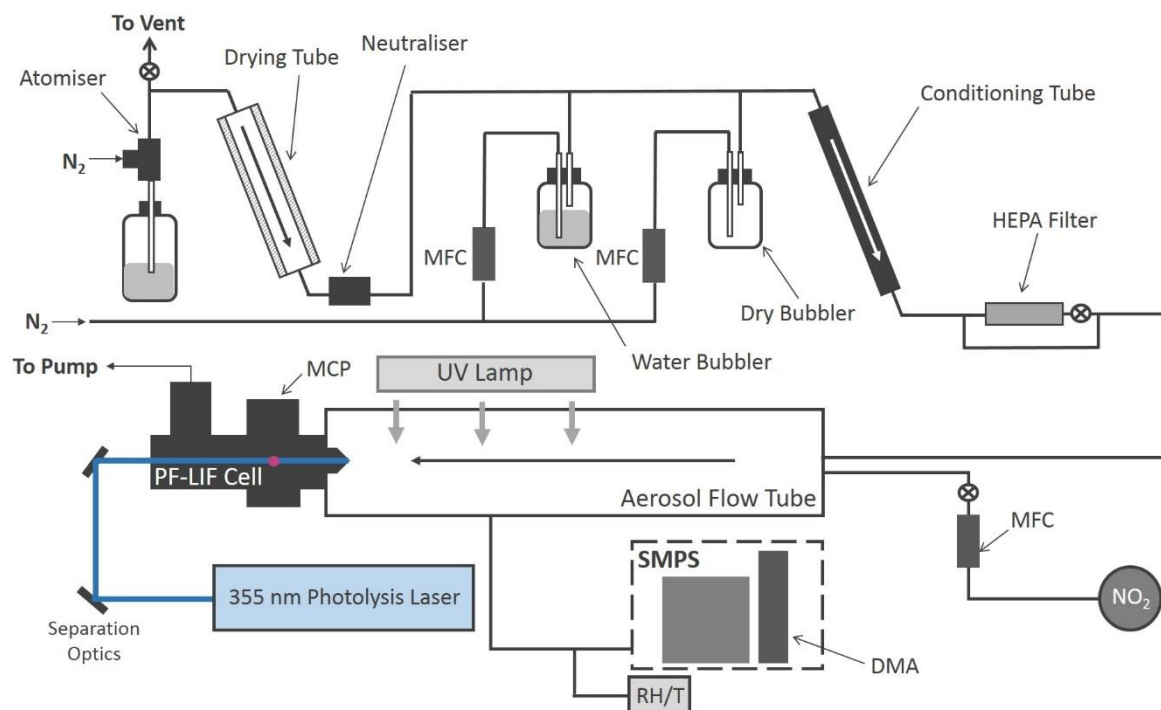
Figure 1. Schematic of the Leeds aerosol flow tube system coupled to a laser-fragmentation laser-induced fluorescence detector for HONO. The paths of the 355 nm (blue) and 308 nm (purple, depicted as travelling out of the page perpendicular to the 355 nm light) light are also shown. CPC: condensation particle counter; DMA: differential mobility analyser; HEPA: high efficiency particle air filter; FAGE: fluorescence assay by gas expansion; MCP: microchannel plate photomultiplier; MFC: mass flow controller; RH/T: relative humidity/ temperature probe; SMPS: scanning mobility particle sizer.

119

120 All experiments were conducted at room temperature (295 ± 3 K) using nitrogen (BOC, 99.998
121 %) or air (BOC, 21 ± 0.5 % O_2) as the carrier gas. A humidified flow of aerosols, ~ 6 lpm (total
122 residence time of 104 s in the flow tube), was introduced through an inlet at the rear of the
123 aerosol flow tube (Quartz, 100 cm long, 5.7511.5 cm ID) which was covered by a black box to
124 eliminate the presence of room light during experiments. A 15 W UV lamp (XX-15LW Bench
125 Lamp, λ_{peak}=365 nm) was situated on the outside of the flow tube to illuminate aerosols and
126 promote the production of HONO (half the length of the flow tube was illuminated leading to
127 an illumination time of 52 s). The concentration of HONO is measured by PF-LIF with
128 sampling from the end of the flow tube via a protruding turret containing a 1 mm diameter
129 pinhole, through which the gas exiting the flow tube was drawn into the detection cell at 5 lpm.
130 The detection cell was kept at low pressure, ~ 1.5 Torr, using a rotary pump (Edwards, E1M80)
131 in combination with a roots blower (Edwards, EH1200). All gas flows in the experiment were

132 controlled using mass flow controllers (MKS and Brooks). The relative humidity (RH) and
133 temperature of the aerosol flow was measured using a probe (Rotronics HC2-S, accuracy ±1
134 % RH) the former calibrated against the H_2O vapour concentration measured by a chilled
135 mirror hygrometer (General Eastern Optica), in the exhaust from the flow tube.

2.2 Aerosol generation and detection

137 Solutions for the generation of TiO_2 aerosol solutions were prepared by dissolving 5 g of
138 titanium dioxide (Aldrich Chemistry 718467, 99.5% Degussa, 80 % anatase: 20 % rutile) into
139 500 ml of milli-Q water. Polydisperse aerosols were then generated from this solution using an
140 atomiser (TSI model 3076) creating a 1 lpm flow of TiO_2 aerosol particles in nitrogen hereafter
141 referred to as the aerosol flow. This aerosol flow was then passed through a silica drying tube
142 (TSI 3062, capable of reducing 60 % RH incoming flow to 20 % RH) to remove water vapour,
143 then passed through a neutraliser to apply a known charge distribution and reduce loss of
144 aerosols to the walls. After the neutraliser the aerosol flow was mixed with both a dry and a
145 humidified N_2 flow (controlled by MFCs) to regulate the relative humidity of the system by
146 changing the ratio of dry to humid nitrogen flows. A conditioning tube was then used to allow
147 for equilibration of water vapour adsorption and re-evaporation to and from the aerosol surfaces
148 for the chosen RH, which was controlled within the range ~10-70 % RH. A portion of the
149 aerosol flow was then passed through a high efficiency particle filter (HEPA) fitted with a
150 bypass loop and bellows valve allowing control of the aerosol number concentration entering
151 the aerosol flow tube. Previous studies (George et al., 2013;Boustead, 2019) have shown the
152 loss of aerosol to the walls of the flow tube to be negligible. Aerosol size distributions were
153 measured for aerosols exiting the flow tube using a scanning mobility particle sizer (SMPS,
154 TSI 3081) and a condensation particle counter (CPC, TSI 3775) which was calibrated using
155 latex beads. Any aerosol surface area not counted due to the upper diameter range of the
156 combined SMPS/CPC (14.6 – 661.2 nm, sheath flow of 3 lpm, instrumental particle counting
157 error of 10-20 %) was corrected for during analysis by assuming a lognormal distribution,
158 which was verified for TiO_2 aerosols generated in this manner (Matthews et al., 2014).
159 However, the majority of aerosols, >90 %, had diameters in the range that could be directly
160 detected. In addition to the experiments with single-component TiO_2, mixed ammonium
161 nitrate/TiO_2 and single-component ammonium nitrate aerosols were also generated using the
162 atomiser for investigations of HONO production from nitrate aerosols without NO_2 present.
163 An example of an aerosol size distribution from this work for single-component ammonium

164 nitrate aerosols, mixed ammonium nitrate/TiO₂ and single-component TiO₂ aerosols is shown

165 in Figure 2.
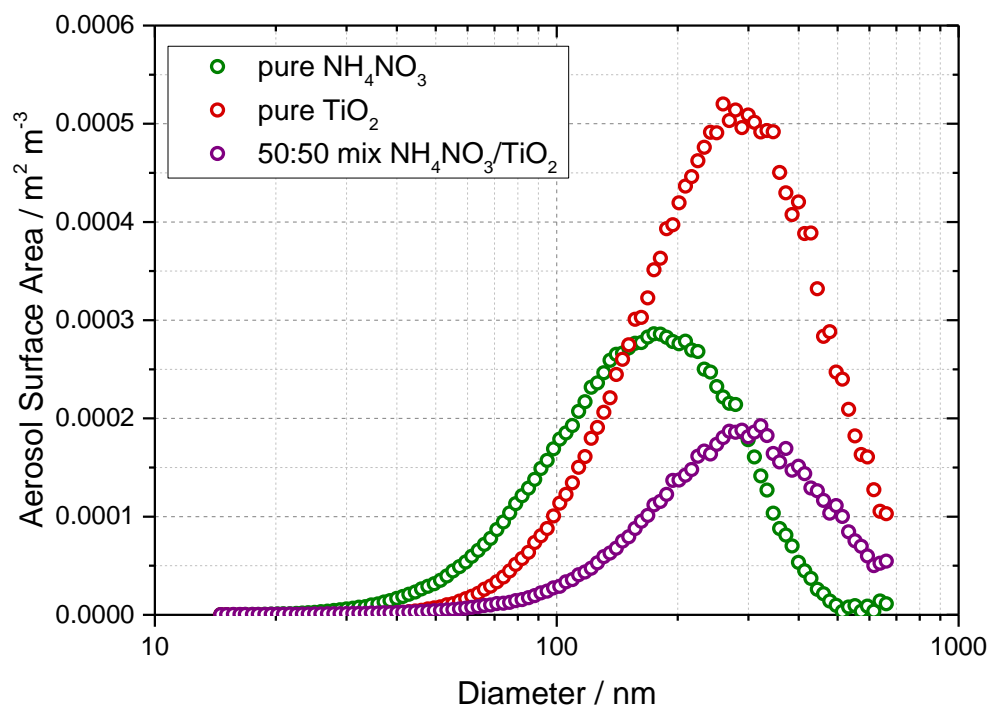
Figure 2 Typical aerosol surface area distribution for pure ammonium nitrate aerosols (green) and pure TiO₂ aerosols (red) and 50:50 mixed nitrate/TiO₂ aerosols (purple) measured after the flow tube.

166 ## 2.3 Detection of HONO

167 As HONO is not directly detectable via LIF, it was necessary to fragment the HONO produced

168 into OH and NO (Liao et al., 2007), with detection of OH via LIF. A 355 nm photolysis laser

169 (Spectron Laser Systems, SL803) with a pulse repetition frequency (PRF) of 10 Hz and pulse

170 duration ~ 10 ns was used to fragment HONO into OH. This fragmentation wavelength was

171 chosen as HONO has a strong absorption peak at ~ 355 nm leading to the breakage of the HO-

172 NO bond to form NO and OH in their electronic ground states (Shan et al., 1989). A Nd:YAG

173 pumped dye probe laser (JDSU Q201-HD, Q-series, Sirah Cobra Stretch) with a PRF of 5000

174 Hz, was used for the detection of OH via the fluorescence assay by gas expansion (FAGE)

175 technique which employs the expansion of gas through a small pinhole into the detection cell.

176 The OH radical was measured using on-resonance detection by LIF via the excitation of the

177 $A\,^2\Sigma^+$ ($v' = 0$) ← $X\,^2\Pi_i$ ($v'' = 0$) Q₁(2) transition at 308 nm (Heard, 2006). A multi-channel plate

178 (MCP) photomultiplier (Photek, MCP 325) equipped with an interference filter at 308 nm (Barr

Associates, 308 nm. FWHM – 8 nm, ~50 % transmission) was used to measure the fluorescence signal. A reference OH cell in which a large LIF signal could be generated was utilised to ensure the wavelength of the probe laser remained tuned to the peak of the OH transition at 308 nm. OH measurements are taken both before and after each photolysis laser pulse allowing measurement of any OH already present in the gas flow to be determined as a background signal for subtraction. The OH generated from HONO photolysis was measured promptly (~800 ns) after the 355 nm pulse to maximise sensitivity to OH before it was spatially diluted away from the measurement region (Boustead, 2019). Offline measurements, with the probe laser wavelength moved away from the OH transition (by 0.02 nm), were taken to allow the signal generated from detector dark counts and scattered laser light to be measured and subtracted from the online signal. To determine an absolute value of the HONO concentration, [HONO], a calibration was performed, in order to convert from the HONO signal, S_{HONO}, using $S_{HONO} = C_{HONO}$ [HONO], as described fully in (Boustead, 2019). A glass calibration wand was used to produce OH and HO_2 in equal concentrations from the photolysis of water vapour at 185 nm:

$$H_2O + h\nu \xrightarrow{\lambda=185\ nm} OH + H \qquad (R7)$$

$$H + O_2 + M \rightarrow HO_2 + M \qquad (R8)$$

An excess flow of NO was then added to generate HONO which was then detected as OH in the cell. The excess flow of NO (BOC, 99.5 %) ensures rapid and complete conversion of OH and HO_2 to HONO. The concentration of OH and HO_2 produced, and therefore the amount of HONO produced in the wand, is calculated using:

$$[OH] = [HO_2] = [H_2O]\ \sigma_{H2O}\ \phi_{OH}\ F\ t \qquad (1)$$

where $[H_2O]$ is the concentration of water vapour in the humidified gas flow, σ_{H2O} is the absorption cross section of H_2O at 185 nm (7.14×10^{-20} cm^2 molecule^{-1} (Cantrell et al., 1997), ϕ_{OH} is the quantum yield of OH for the photo-dissociation of H_2O at 185 nm (=1), F is the lamp flux and t is the irradiation time (the product of which is determined using ozone actinometry (Boustead, 2019).

A typical value of the calibration factor was $C_{HONO} = (3.63 \pm 0.51) \times 10^{-9}$ counts mW^{-1} for N_2, leading to a calculated limit of detection of 12 ppt for a 50 s averaging period and a signal-to-noise ratio (SNR) of 1 (Boustead, 2019). The typical error in the HONO concentration was 15% at 1σ, determined by the error in the calibration.

2.4 Experimental procedure and data analysis

The experiments were performed with a minimum flow of 6 lpm through the aerosol flow tube giving a Reynolds number of ~ 150 which ensured a laminar flow regime. The HONO signal, converted to an absolute concentration using a calibration factor, was measured over a range of aerosol surface area densities, both in the presence and absence of illumination, and background measurements without aerosols present, were also performed.

The HONO signal originates from several sources: the illuminated aerosol surface; the illuminated quartz flow tube walls; dark reactions on aerosol surfaces; dark reactions on the flow tube surface and finally from impurities in the NO_2 (Sigma Aldrich, >99.5 %, freeze pump thawed to further remove any remaining NO or O_2) and N_2 flows (either HONO itself or a species which photolyses at 355 nm to give OH). Of interest here is the HONO production from both dark and illuminated aerosol surfaces which is atmospherically relevant. Following transit through the flow tube, and in the presence of NO_2, the total concentration of HONO measured by the PF-LIF detector is given by:

$$[HONO] = [HONO]_{illuminated\ aerosols} + [HONO]_{illuminated\ walls}$$
$$+ [HONO]_{dark\ aerosols} + [HONO]_{dark\ walls} + [HONO]_{impurities} \quad (2)$$

Any HONO seen without the presence of aerosol was therefore due to HONO impurities in the N_2 or NO_2 gas, the dark production of HONO from the flow tube walls or from the production of HONO from the illuminated reactor walls, which may include production from TiO_2 aerosols coating the flow tube in the presence of NO_2. This background HONO concentration depended on the experimental conditions and on how recently the flow tube and PF-LIF cell had been cleaned to remove any build-up of TiO_2 deposits. However, the build-up of TiO_2 on the flow tube walls was relatively slow and back-to-back measurements were made in the presence and absence of aerosols to obtain an accurate background. Additional experiments showed no significant production of HONO on TiO_2 aerosol surfaces without the presence of NO_2. Even though the aerosol surface area density (~0.02 $m^2\,m^{-3}$) was small compared to the surface area density of the reactor walls (35 $m^2\,m^{-3}$), very little HONO signal was produced without the presence of aerosols, and was always subtracted from the signal in the presence of aerosols. The HONO signal was measured both with the lamp on and off for each aerosol surface area density to investigate the production of HONO from illuminated aerosol surfaces. The HONO signal was averaged over 50 s (average of 500 of the 355 nm photolysis laser pulses with a PRF of 10 Hz). Once aerosols were introduced into the flow tube system a period of ~

237   30 min was allowed for equilibration and the measured aerosol surface area density to stabilise.

238   In general, the relative humidity of the system was kept constant at RH ~ 15 % for all

239   experiments investigating HONO production as a function of NO_2 mixing ratio over the range

240   34 - 400 ppb. In a number of experiments, however, RH was varied in the range ~12-37 %.

241   The mixing ratio of NO_2 entering the flow tube was calculated using the concentration of the

242   NO_2 in the cylinder and the degree of dilution. The NO_2 mixing ratio within the cylinder was

243   determined using a commercial instrument based on UV-Vis absorption spectroscopy (Thermo

244   Fisher 42TL, limit of detection 50 pptv, precision 25 pptv) For each individual experiment, the

245   mixing ratio of NO_2 was kept constant (within the range 34 – 400 ppb) and the aerosol surface

246   area density was varied from zero up to a maximum of 0.04 $m^2\,m^{-3}$. In order to obtain the

247   HONO produced from illuminated aerosol surfaces in the flow tube for a given mixing ratio of

248   NO_2. As well as subtraction of any background HONO, a correction must be made for any loss

249   of HONO owing to its photolysis occurring within the flow tube.

250   In order to determine the rate of photolysis of HONO, the rate of photolysis of NO_2 was first

251   determined using chemical actinometry, and the known spectral output of the lamp and the

252   literature values of the absorption cross-sections and photo-dissociation quantum yields for

253   NO_2 and HONO were used to determine the rate of photolysis of HONO. When just flowing

254   NO_2 in the flow tube, the loss of NO_2 within the illuminated region is determined only by

255   photolysis and is given by:

$$-\frac{d[NO_2]}{dt} = j(NO_2)[NO_2] \tag{3}$$

256   where $j(NO_2)$ is the photolysis frequency of NO_2 for the lamp used in these experiments. From

257   the measured loss of NO_2 in the illuminated region, and with knowledge of the residence time,

258   the photolysis frequency, $j(NO_2)$, was determined to be $(6.43 \pm 0.30) \times 10^{-3}\,s^{-1}$ for the set of

259   experiments using one lamp to illuminate the flow tube. $j(NO_2)$ is given by:

$$j(NO_2) = \int_{\lambda_1}^{\lambda_2} \sigma_\lambda \phi_\lambda F_\lambda \, d\lambda \tag{4}$$

260   where λ_1 and λ_2 represent the range of wavelengths over which the lamp emits, and σ_λ and ϕ_λ

261   are the wavelength-dependent absorption-cross section and photo-dissociation quantum yield

262   of NO_2, respectively, and F_λ is the flux of the lamp at a given wavelength. The flux of the lamp,

the spectral intensity of which was measured using a Spectral Radiometer (Ocean Optics QE-Pro 500) as a function of wavelength, is shown in Figure 3.

.
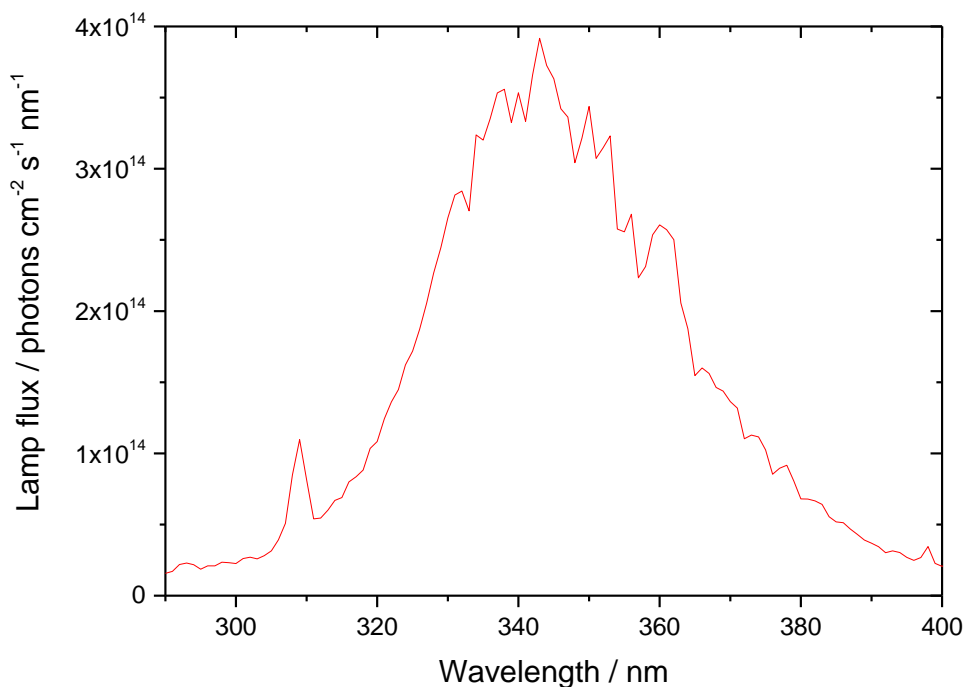
Figure 3. UVA emission spectrum for the 15 W bench lamp used in these experiments between 290-400 nm. The integrated photon flux over this wavelength range is $(1.63 \pm 0.09) \times 10^{16}$ photons cm^{-2} s^{-1} determined from the measured $j(NO_2)$ of $(6.43 \pm 0.30) \times 10^{-3}$ s^{-1}.

From the measured $j(NO_2)$, and with knowledge of σ_λ and ϕ_λ for NO_2, the flux of the lamp was determined to be $(1.63 \pm 0.09) \times 10^{16}$ photons cm^{-2} s^{-1} integrated over the $290 - 400$ nm wavelength range of the lamp. Using this flux, and the known σ_λ and ϕ_λ for HONO over the same wavelength range, $j(HONO)$ was determined to be $(1.66 \pm 0.10) \times 10^{-3}$ s^{-1}.

In the presence of aerosols under illuminated conditions, the rate of heterogeneous removal of NO_2 at the aerosol surface to generate HONO is given by:

$$-\frac{d[NO_2]}{dt} = k[NO_2] \tag{5}$$

where k is the pseudo-first order rate coefficient for loss of NO_2 at the aerosol surface, and which leads to the generation of HONO. The postulated mechanism for HONO production from NO_2 is discussed in section 3.3.2 below, but for the definition of k it is assumed to be a first order process for NO_2. Integration of equation 5 gives:

$$k = -\frac{\ln(\frac{[NO_2]_0 - [HONO]_t}{[NO_2]_0})}{t} \tag{6}$$

where $[NO_2]_0 - [HONO]_t$ is the concentration of NO_2 at time t, assuming that each NO_2 molecule is quantitatively converted to a HONO molecule following surface uptake (see section 3.3.2 for the proposed mechanism), and $[NO_2]_0$ is the initial concentration of NO_2. Hence k can be determined from equation 6 using the measurement of the concentration of HONO, [HONO], that has been generated from TiO_2 aerosol surfaces for an illumination time of t (and after subtraction of any background HONO produced from other sources and after correction for loss via photolysis, see above), and with knowledge of $[NO_2]_0$.

The reactive uptake coefficient of NO_2 to generate HONO, $\gamma_{NO_2 \rightarrow HONO}$, defined as the probability that upon collision of NO_2 with the TiO_2 aerosol surface a gas-phase HONO molecule is generated, is given by:

$$\gamma_{NO_2 \rightarrow HONO} = \frac{4 \times k}{v \times SA} \tag{7}$$

where v is the mean thermal velocity of NO_2, given by $v = \sqrt{(8RT/(\pi M)}$ with R, T and M as the gas constant, the absolute temperature and the molar mass of NO_2, respectively, SA is the aerosol surface area density ($m^2\,m^{-3}$) and k is defined as above. Rearrangement of equation 7 gives:

$$k = \frac{\gamma_{NO_2 \rightarrow HONO} \times SA \times v}{4} \tag{8}$$

Figure 4 shows the variation of k, determined from equation 6 above with $t = 52$ s (illumination time in the flow tube), against aerosol surface area density, SA, for $[NO_2]_0 = 200$ ppb and RH=15%, from which the gradient using equation 8 yields $\gamma_{NO_2 \rightarrow HONO} = (2.17 \pm 0.09) \times 10^{-5}$.
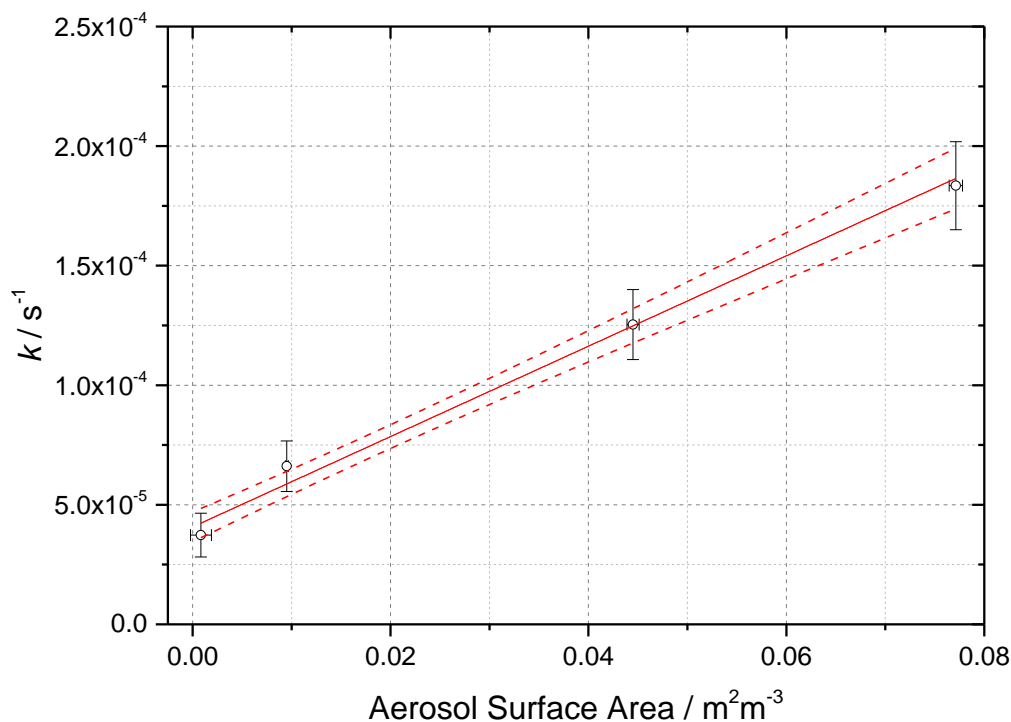
Figure 4. Pseudo-first-order rate coefficient for HONO production, k (open circles) as a function of aerosol surface area for $[NO_2] = 200$ ppb and RH=15 ± 1 %, T = 293 ± 3 K and a photolysis time of 52 ± 2 seconds. The red line is a linear-least squared fit including 1σ confidence bands (dashed lines) weighted to both x and y errors (1σ), the gradient of which yields $\gamma_{NO_2 \rightarrow HONO} = (2.17 \pm 0.09) \times 10^{-5}$, with the uncertainty representing (1σ). The non-zero y-axis intercept is due to a background HONO signal owing to the presence of a HONO impurity in the NO_2 cylinder, and which is not subtracted. The total photon flux of the lamp (see Figure 2 for its spectral output) = $(1.63 \pm 0.09) \times 10^{16}$ photons cm^{-2} s^{-1}.

292   The uncertainty in k (~20 %) shown in Figure 4 and determined by equation 6 is mainly
293   controlled by the uncertainty in the HONO concentration (the HONO signal typically varies
294   between repeated runs for a given SA by ~ 10 % coupled with the 15 % error in calibration
295   factor), the initial NO_2 mixing ratio (10%), and the photolysis time, t (~3 %). The uncertainty
296   in SA is determined by the uncertainty in the SMPS (15%). The error in the value of
297   $\gamma_{NO_2 \rightarrow HONO}$ (typically 20%) is calculated from the 1σ statistical error of the weighted fit shown
298   in Figure 4. An experiment performed using air yielded an uptake coefficient value within 7 %
299   of the equivalent experiment done in N_2, which is well within the experimental error.

300   ## 2.5   Box model description

301   A kinetic scheme within the framework of a box model was used together with the differential
302   equation solver Facsimile 4.3.53 (MCPA software Ltd., 2020) to investigate the mechanism of

303   NO_2 adsorption on TiO_2 in the presence of light to produce HONO. The models were only

304   semi-explicit, focusing on determining the stoichiometric amounts of NO_2 needed to produce

305   a single HONO molecule in the gas-phase for comparison with the experimental dependence

306   of HONO production upon NO_2 mixing ratio, and to provide a predictive framework for

307   parameterising the HONO production rate with NO_2 mixing ratio in the atmosphere. Three

308   model scenarios were designed. The simplest model (Model 1) considered only the adsorption

309   of a single molecule of NO_2 to the TiO_2 surface, the surface conversion to HONO in the

310   presence of light and subsequent desorption of HONO, the latter assumed to occur rapidly. The

311   two further model scenarios investigated the effect of a 2:1 stoichiometric relationship between

312   the NO_2 adsorbed to the surface of TiO_2 and the HONO produced, via the formation of an NO_2

313   dimer. Model 2 incorporated an Eley-Rideal mechanism reliant on the adsorption of one NO_2

314   molecule to the surface followed by the subsequent adsorption of a second NO_2 molecule

315   directly onto the first (Figure 5). Model 3, however, features a Langmuir-Hinshelwood

316   mechanism of adsorption in which two NO_2 molecules adsorb to the surface, then diffuse to

317   one another before colliding on the surface and forming the *cis*-ONO-NO_2 dimer (Finlayson-

318   Pitts et al., 2003;de Jesus Madeiros and Pimentel, 2011;Liu and Goddard, 2012;Varner et al.,

319   2014). The formation of the asymmetric *cis*-ONO-NO_2 dimer followed by isomerisation to

320   form the asymmetric *trans*-ONO-NO_2 dimer has been suggested to have an enthalpic barrier

321   that is ~170 kJ mol^{-1} lower than for direct isomerisation to *trans*-ONO-NO_2 from the symmetric

322   N_2O_4 dimer (Liu and Goddard, 2012). The dimerisation of NO_2 and subsequent isomerisation

323   to form *trans*-ONO-NO_2 has been suggested under dark conditions to lead to the formation of

324   both HONO and HNO_3 in the presence of water vapour (Finlayson-Pitts et al., 2003;de Jesus

325   Madeiros and Pimentel, 2011;Liu and Goddard, 2012;Varner et al., 2014). Although the

326   interaction of light with TiO_2 with the concomitant production of electron-hole pairs (R1) is

327   central to HONO formation, we do not specify here the exact mechanism by which the electron-

328   hole pairs interact with surface-bound species to generate HONO. We propose that the

329   interaction with light speeds up the autoionisation of *trans*-ONO-NO_2 to form $(NO^+)(NO_3^-)$,

330   which is represented by reactions R13 and R15 in Models 2 and 3 respectively. $(NO^+)(NO_3^-)$

331   can then react rapidly with surface adsorbed water leading to HONO formation (Varner et al.,

332   2014).

333   A schematic of the proposed mechanism investigated with Models 2 and 3 is shown in Figure

334   5, and consists of (i) the adsorption of NO_2 onto a surface site, (ii) the conversion of NO_2 to

335   form HONO via the formation of an NO_2 dimer intermediate on the surface via either a Eley-

336 Rideal or Langmiur Hinshelwood- type mechanism, (iii) subsequent desorption of HONO from

337 the surface, and finally (iv) competitive removal processes for HONO both on the surface and

338 in the gas-phase that are either dependent or independent on the NO_2 mixing ratio. The model

339 includes the gas-phase photolysis of NO_2 and HONO and the gas phase reactions of both

340 HONO and NO_2 with OH and $O(^3P)$ atoms.
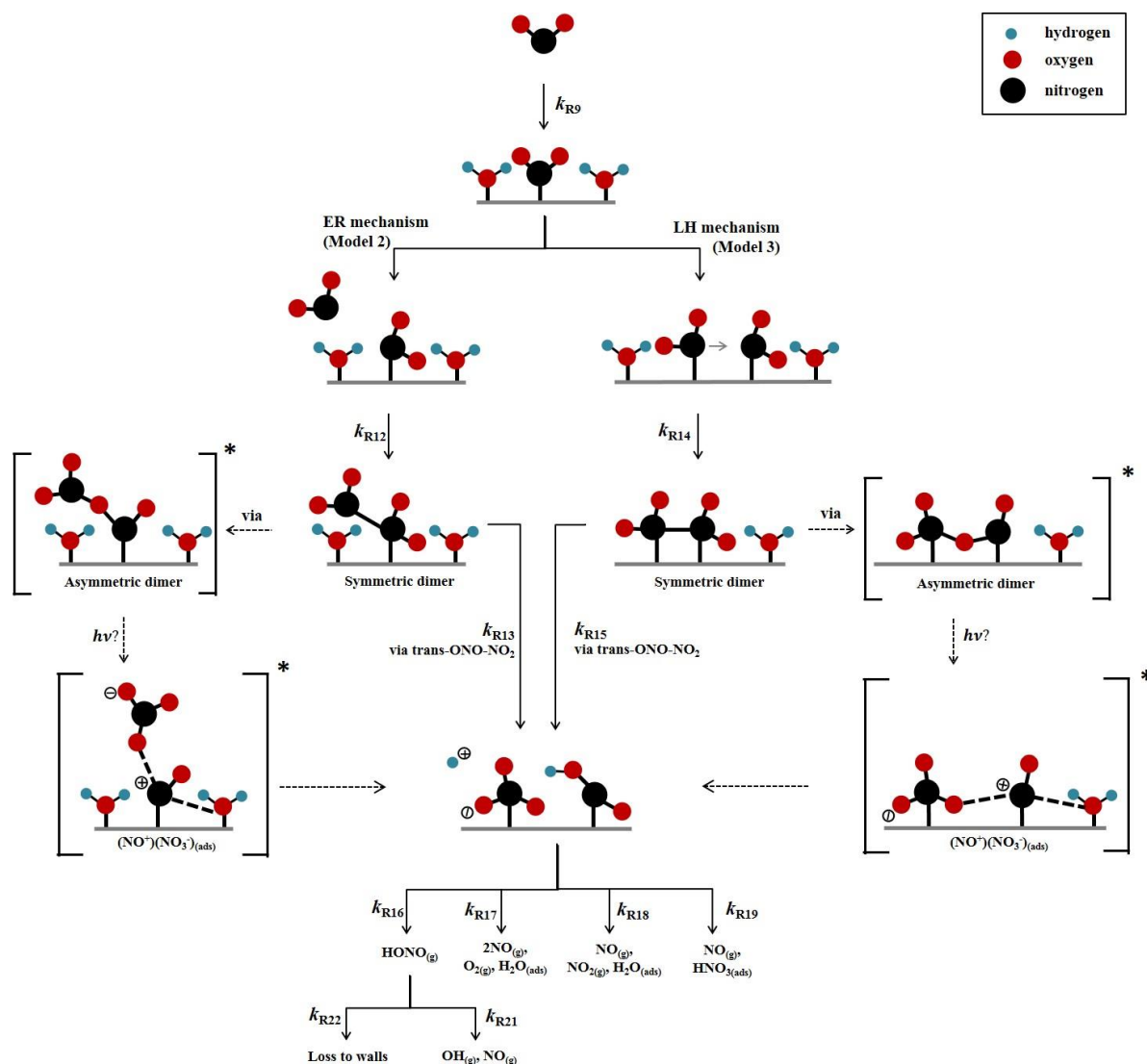
Figure 5. Schematic diagram of proposed mechanism of uptake of NO_2 on an aerosol surface in the presence of water to form HONO. Both Eley Rideal, Model 2, and Langmuir Hinshelwood, Model 3, mechanisms are shown with relevant estimated and calculated rate coefficients used in the models. NO_2 dependent and independent loss reactions of HONO are also depicted. Nitrogen shown in black, oxygen shown in red and hydrogen shown in blue. * denotes intermediate steps of the isomerisation of symmetric N_2O_4 to *trans*-ONO-NO_2 which is then predicted to form HONO.

341 To the best of our knowledge the enthalpy of adsorption of NO_2 onto a TiO_2 surface has not

342 been determined, nor the bimolecular rate coefficients for the chemical steps on the surface

shown in Figure 5. Hence, for each of the steps a rate coefficient (s^{-1} or cm^3 molecule^{-1} s^{-1}) was assigned, as given in Table 1, and with the exception of the experimentally determined $j(NO_2)$ and the calculated $j(HONO)$, and the gas-phase rate coefficients which are known, the rate coefficients were estimated, with the aim of reproducing the experimental NO_2 dependence of the HONO production and NO_2 reactive uptake coefficient; justification of chosen values is given below.

Reactions		Rate coefficient[d]
Model 1		
R9	$NO_{2(g)} + surface \rightarrow NO_{2(ads)}$	1×10^{-3}
R10	$NO_{2(ads)} \rightarrow HONO_{(ads)}$	1×10^{-3}
R11	$HONO_{(ads)} \rightarrow HONO_{(g)}$	1×10^{-2}
Model 2 and 3		
Model 2 only – Eley-Rideal mechanism		
R12	$NO_{2(g)} + NO_{2(ads)} \rightarrow NO_2 - NO_{2(ads)}$	1×10^{-2}
R13	$NO_2 - NO_{2(ads)} \xrightarrow{via\ trans-ONO-NO_2} HONO_{(ads)} + HNO_{3(ads)}$	5×10^{-3}
Model 3 only – Langmuir-Hinshelwood mechanism		
R14	$NO_{2(ads)} + NO_{2(ads)} \rightarrow NO_{2(ads)} - NO_{2(ads)}$	1×10^{-3}
R15	$NO_{2(ads)} - NO_{2(ads)} \xrightarrow{via\ trans-ONO-NO_2} HONO_{(ads)} + HNO_{3(ads)}$	5×10^{-3}
Common to both Models 2 and 3		
R9	$NO_{2(g)} + surface \rightarrow NO_{2(ads)}$	1×10^{-1}
R16	$HONO_{(ads)} \rightarrow HONO_{(g)}$	5×10^{-2}
R17	$HNO_{3(ads)} + HONO_{(ads)} \rightarrow 2NO_{(g)} + O_{2(g)} + H_2O_{(ads)}$	1×10^{-3}
R18	$HONO_{(ads)} + HONO_{(ads)} \rightarrow NO_{(g)} + NO_{2(g)} + H_2O_{(ads)}$	1×10^{-3}
R19	$NO_{2(g)}(or\ species\ such\ as\ NO_2^+) + HONO_{(ads)} \rightarrow NO_{(g)} + HNO_{3(ads)}$	5×10^{-3}
R20	$NO_{2(g)} + h\nu \rightarrow NO_{(g)} + O(^3P)_{(g)}$	6×10^{-3a}
R21	$HONO_{(g)} + h\nu \rightarrow OH_{(g)} + NO_{(g)}$	2×10^{-3b}
R22	$HONO_{(g)} \rightarrow wall\ loss$	1×10^{-4}
R23	$HONO_{(g)} + OH_{(g)} \rightarrow NO_{2(g)} + H_2O_{(g)}$	4.5×10^{-12c}
R24	$NO_{2(g)} + OH_{(g)} \xrightarrow{M} HNO_{3(g)}$	1×10^{-11c}
R25	$O(^3P)_{(g)} + NO_{2(g)} \rightarrow O_{2(g)} + NO_{(g)}$	1×10^{-11c}
R26	$O(^3P)_{(g)} + O_{2(g)} \xrightarrow{M} O_3$	1.5×10^{-14c}
R27	$O(^3P)_{(g)} + NO_{(g)} \xrightarrow{M} NO_{2(g)}$	1.7×10^{-12c}

Table 1. Reactions included in the chemical mechanism used to model NO_2 uptake onto TiO_2 aerosols. All rate coefficients are estimated, as described in Section 2.5, with the exception of the NO_2 and HONO photolysis rate coefficient and the gas phase rate coefficient which are known. [a]Measured using chemical actinometry with the

352   knowledge of the experimentally determined spectral output of the lamp and the cross-sections and quantum

353   yields of NO_2 and HONO, see section 2.4 for more detail. [b]Calculated using a photon flux of $(1.63 \pm 0.09) \times$

354   10^{16} photons cm^{-2} s^{-1}.[c](Sander et al., 2003). [d]Rate coefficients are in the units of s^{-1} for first-order processes or

355   cm^3 molecule^{-1} s^{-1} for second-order processes. T for all k values is 298 K.

356   The modelled Gibbs free energy barrier for the isomerisation of N_2O_4 to form the asymmetric

357   ONO-NO_2 isomer (*cis* or *trans* conformation not specified) was estimated by Pimental et al.,

358   (2007) to be 87 kJ mol^{-1} with a rate coefficient as large as 2×10^{-3} s^{-1} in the aqueous phase at

359   298 K, stated in the study to confirm the Finlayson-Pitts model for the hydrolysis of NO_2 on

360   surfaces via the asymmetric *trans*-ONO-NO_2 dimer (Finlayson-Pitts et al., 2003). Using this

361   study as a guide, we estimated k_{R13} and k_{R15} as 5×10^{-3} s^{-1}, slightly larger than that estimated

362   by Pimental et al., (2007) due to the presence of light. A study into the decomposition of HONO

363   on borosilicate glass surfaces suggested a rate coefficient for the loss HONO on the non-

364   conditioned chamber walls to be $(1.0 \pm 0.2) \times 10^{-4}$ s^{-1} increasing to $(3.9 \pm 1.1) \times 10^{-4}$ s^{-1} when

365   HNO_3 was present on the walls (Syomin and Finlayson-Pitts, 2003). From this we estimated a

366   light-accelerated loss rate coefficient of 1×10^{-3} s^{-1} for the loss of HONO$_{(ads)}$ by reaction with

367   itself, k_{R18}, and through reaction with $HNO_{3(ads)}$, k_{R17}. Both these reactions will occur on the

368   surface of the aerosol. We make the assumption that the rate of loss of HONO to the walls of

369   the chamber for this experiment is less than that of the heterogeneous loss reactions on the

370   photo-catalytic aerosol surface leading to a k_{R22} of 1×10^{-4} s^{-1} as reported by (Syomin and

371   Finlayson-Pitts, 2003)**.** For k_{R12}-k_{R15}, initial values were adopted and were then adjusted to fit

372   the shape of the trend in experimental results of [HONO] and $\gamma_{NO_2 \rightarrow HONO}$ versus [NO_2],

373   discussed fully in Section 3.3.2. For completeness, gas-phase loss reactions of HONO and NO_2

374   with OH and the reactions of O(^{3}P) with NO, NO_2 and O_2 were also included in the model,

375   R23-R27, though their inclusion had no effect on the HONO concentration. The rates of R23-

376   R27 within the model are much smaller than HONO loss reactions on the surface (R17-R19)

377   and the photolysis reactions (R21). For both Models 2 and 3, the adsorption of an NO_2 molecule

378   to the surface, k_{R9}, was assumed to be rapid and not the rate determining step. Likewise, the

379   desorption of HONO was also assumed to be rapid, faster than the loss rates of adsorbed HONO

380   but slower than the adsorption of NO_2; this was necessary for the model to reproduce the trend

381   in the experimental results of [HONO] versus [NO_2], discussed fully in Section 3.3.2.

3   Results and Discussion

3.1   HONO production from TiO₂ aerosol surfaces in the presence of NO₂

The production of HONO on TiO_2 aerosol surfaces was measured as a function of the initial NO_2 mixing ratio. Figure 6 shows the dependence of the HONO concentration, measured at the end of the flow tube, on the initial NO_2 mixing ratio for an aerosol surface area of $(1.6 \pm 0.8) \times 10^{-2}$ m^2 m^{-3}. A sharp increase in HONO production at a low mixing ratio of NO_2 was seen followed by a more gradual reduction in HONO production after a peak production at ~ 54 ± 5 ppb NO_2.
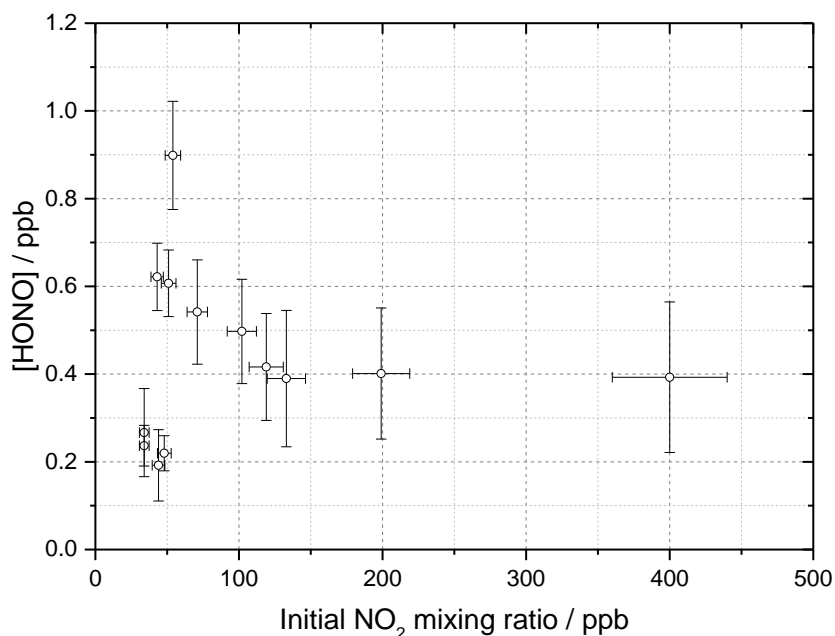
Figure 6. HONO concentration measured at the end of the flow tube as a function of the initial NO_2 mixing ratio, for the aerosol surface area density of $(1.6 \pm 0.8) \times 10^{-2}$ m^2 m^{-3}, relative humidity 15 ± 1 %, photon flux $(1.63 \pm 0.09) \times 10^{16}$ photons cm^{-2} s^{-1} (290-400 nm wavelength range), reaction time of 52 seconds and N_2 carrier gas. Each point is an average of up to 20 measurements at the same aerosol surface area and mixing ratio of NO_2. The highest concentration of HONO measured was 0.90 ± 0.12 ppb at $[NO_2] = 54 \pm 5$ ppb. The y error bars represent 1σ while the x error bars represent the sum in quadrature of the errors in the N_2 and NO_2 gas flows and the NO_2 dilution. The SA varied over the experiments at different NO_2 mixing ratios leading to a larger error in the quoted SA.

Figure 7 shows the HONO concentration measured at the end of the flow tube over a range of RH values for a fixed aerosol surface area density of $(1.59 \pm 0.16 \times 10^{-2}$ m^2 $m^{-3})$ and at two

392 NO₂ mixing ratios, displaying a peak in HONO production between 25 – 30 % RH. Above ~

393 37 % RH, for experiments including single-component TiO₂ aerosols, it was found that

394 significant aerosols were lost from the system before entering the flow tube, speculated to be

395 due to loss to the walls of the Teflon lines. As such the RH dependence was only studied up to

396 37 % RH, however a clear drop off in HONO production was seen for both NO₂ mixing ratios

397 studied after ~ 30 % RH.
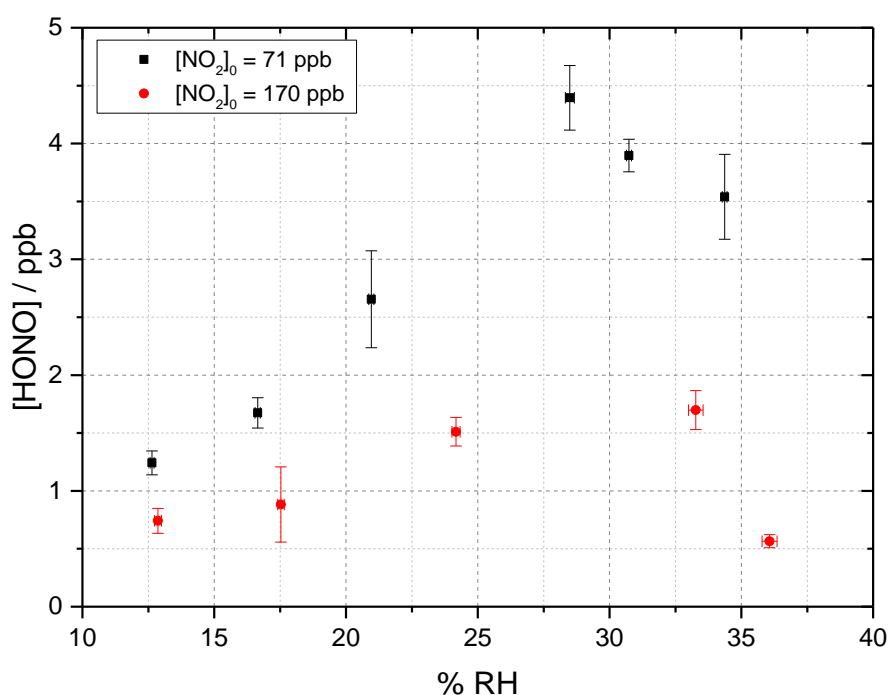
Figure 7. RH dependence of HONO production from illuminated TiO₂ aerosol surfaces at 295 K in N₂ at 71 (black) and 170 (red) ppb initial NO₂ mixing ratio. The aerosol surface area density was kept constant at $(1.59 \pm 0.16) \times 10^{-2}$ m² m⁻³ with a photon flux of $(1.63 \pm 0.09) \times 10^{16}$ photons cm⁻² s⁻¹ and an illumination time of 52 ± 2 seconds. The error bars represent 1σ.

398 A dependence of HONO production upon RH was expected due to the potential role of water

399 as a proton donor in the production mechanism of HONO on TiO₂ surfaces (R2) and (R5), as

400 shown in Figure 5 (Dupart et al., 2014). The fractional surface coverage of water on the TiO₂

401 aerosol core, *V/Vₘ*, at 15 % RH and above was calculated using the parameterisation below,

402 which was determined using transmission IR spectroscopy (Goodman et al., 2001):

$$\frac{V}{V_m} = \left[\frac{c\left(\frac{P}{P_0}\right)}{1 - \left(\frac{P}{P_0}\right)}\right]\left[\frac{1 - (n+1)\left(\frac{P}{P_0}\right)^n + n\left(\frac{P}{P_0}\right)^{n+1}}{1 + (c-1)\left(\frac{P}{P_0}\right) - c\left(\frac{P}{P_0}\right)^{n+1}}\right] \tag{9}$$

where V is the volume of water vapour adsorbed at equilibrium pressure P, V_m is the volume of gas necessary to cover the surface of TiO_2 particles with a complete monolayer, P_0 is the saturation vapour pressure, c is the temperature dependent constant related to the enthalpies of adsorption of the first and higher layers (taken as 74.8 kJ mol^{-1} for TiO_2 (Goodman et al., 2001)) and n is the asymptotic limit of monolayers (8 for TiO_2 (Goodman et al., 2001)) at large values of P/P_0.

At 15 % RH, a fractional water coverage of 1.09 was calculated to be present on the surface, increasing to 1.50 at 35 % RH. It has been shown in previous work that HONO can be displaced from a surface by water, leading to an increase in gas-phase HONO with RH (Syomin and Finlayson-Pitts, 2003). The increase in HONO with RH to ~25-30 % RH could therefore be attributed to both an increase in the concentration of the water reactant leading to more HONO formation and the increase in displacement of HONO from the surface due to preferential adsorption of water. A decrease in HONO production seems to occur above ~ 30 % RH, which could be due to the increased water adsorption inhibiting either NO_2 adsorption or the electron/hole transfer process (Gustafsson et al., 2006). H_2O vapour adsorption is likely enhanced by the superhydrophilic properties of TiO_2 surfaces under UV radiation meaning that water monolayers form more quickly on the surface of TiO_2 owing to light-induced changes in surface tension (Takeuchi et al., 2005;Gustafsson et al., 2006).

At the higher initial concentration of NO_2 = 170 ppb, the RH dependence showed a similar peak in HONO production between ~25 - 30 % RH but less HONO was produced overall, as expected from Figure 6 given the higher NO_2. Previous work on the production of HONO from suspended TiO_2 aerosols reported a strong RH dependence of the uptake coefficient, γ, of NO_2 to form HONO with a peak at ~ 15 % RH and decreasing at larger RH (Gustafsson et al., 2006). The same trend for the NO_2 uptake coefficient was observed by Dupart et al., 2014 on Arizona test dust (ATD) aerosols with a peak in γ at ~ 25 % RH. This increase in the RH at which the uptake coefficient for NO_2 in going from TiO_2 to ATD aerosols was ascribed to the lower concentration of TiO_2 present in ATD aerosols as opposed to single-component TiO_2 aerosols used by Gustafsson et al., 2006 as well as by differences in particle size distribution. Gustafsson et al., 2006 reported a larger aerosol size distribution with a bimodal trend with mode diameters

of ~ 80 and ~ 350 nm for single-component TiO_2 aerosols whereas Dupart et al., 2014 reported a smaller unimodal aerosol size distribution for ATD aerosols with a mode diameter of ~110 nm. In this work we also see a larger aerosol size distribution, with a lower mode diameter of ~ 180 nm similar to Dupart et al., 2014 but for pure TiO_2 aerosols; aerosol size distribution shown in Figure 2. Similar to the results of Dupart et al., 2014 we observe a trend inversion in [HONO] vs RH at higher RH, between 25-30 %. An increase in HONO as a function of RH has also been observed on TiO_2 containing surfaces (Langridge et al., 2009;Gandolfo et al., 2015;Gandolfo et al., 2017) with a similar profile for the observed RH dependence of HONO being observed by Gandolfo et al., (2015) from photo-catalytic paint surfaces with a maximum in HONO mixing ratio found at 30 % RH. In comparison, a study focusing on the products of the uptake of NO_2 on TiO_2 surfaces showed a maximum in the gas-phase HONO yield at 5 % RH with the yield of HONO plateauing off with further increase in humidity (Bedjanian and El Zein, 2012).

3.2 Dependence of reactive uptake coefficient on initial NO₂ mixing ratio

The reactive uptake coefficient, $\gamma_{NO_2 \rightarrow HONO}$ for $NO_2 \rightarrow HONO$ on TiO_2 aerosol particles was determined experimentally for 18 different initial NO_2 mixing ratios, and is shown in Figure 8. For each initial NO_2 mixing ratio, the gradient of the first order rate coefficient for HONO production, k, as a function of aerosol surface area density (e.g. Figure 4) and in conjunction with equation 8, was used to obtain $\gamma_{NO_2 \rightarrow HONO}$. The uptake coefficient initially increases with NO_2, reaching a peak at $\gamma_{NO_2 \rightarrow HONO} = (1.26 \pm 0.17) \times 10^{-4}$ for an initial NO_2 mixing ratio of 51 ± 5 ppb, before sharply decreasing as the NO_2 mixing ratio continues to increase above this value.
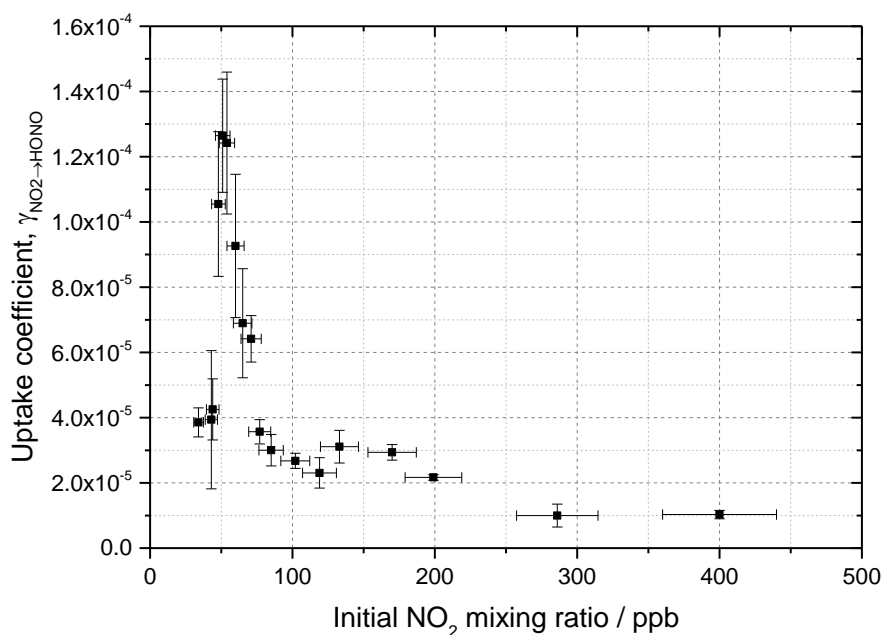
Figure 8 Experimental results showing the reactive uptake coefficients of NO_2 to form HONO, $\gamma_{HONO \to NO_2}$ onto TiO_2 aerosol surfaces as a function of the initial NO_2 mixing ratio. All experiments were conducted in N_2 at 295 K at 15 ± 1 % RH, a photon flux of $(1.63 \pm 0.09) \times 10^{16}$ photons cm^{-2} s^{-1} and an illumination time of 52 ± 2 seconds. $\gamma_{HONO \to NO_2}$ was determined for each NO_2 mixing ratio from the gradient of the pseudo-first-order rate coefficient for HONO production, k, versus aerosol surface area density varied from 0 - 0.04 m^2 m^{-3} (e.g. as shown in Figure 4) and equation 8.

454   The increase in uptake coefficient with NO_2 at low NO_2 (< 51 ppb) has not been seen previously
455   in studies of HONO production from TiO_2 containing aerosols with similar $[NO_2]$ ranges
456   (Gustafsson et al., 2006;Ndour et al., 2008;Dupart et al., 2014) nor with other aerosol surfaces
457   (Bröske et al., 2003;Stemmler et al., 2007) or TiO$_2$ surfaces (El Zein and Bedjanian, 2012b). It
458   is worth noting that several of these studies reported the overall uptake of NO_2 onto aerosol
459   surfaces and not specifically the uptake to form HONO, although HONO was indirectly
460   measured in all studies noted here (Gustafsson et al., 2006;Ndour et al., 2008;Dupart et al.,
461   2014). For single-component TiO_2 aerosols, Gustafsson et al., (2006) reported a uptake
462   coefficient, γ_{NO_2}, of 9.6×10^{-4} at 15 % RH and 100 ppb NO_2. Taking into account the HONO
463   yield of 0.75 given by (Gustafsson et al., 2006), an estimated $\gamma_{NO_2 \to HONO} = 7.2 \times 10^{-4}$ is
464   determined and can be compared to the value observed in this work at 15 % RH and 100 ppb
465   NO_2, ($\gamma_{NO_2 \to HONO} = (2.68 \pm 0.23) \times 10^{-5}$). The $\gamma_{NO_2 \to HONO}$ we determine is 27 times smaller
466   than reported by Gustafsson et al., (2006). This difference is mostly due to the lower
467   experimental photon flux in our setup, ~19 times less at $\lambda_{max} = 365$ nm owing to the use of

468 one 15 W UV lamp to irradiate the flow tube (Boustead, 2019) compared to Gustafsson et al.,

469 2006 which utilised four 18 W UV lamps.

470 The origins of the increase in $\gamma_{NO_2 \rightarrow HONO}$, together with reaching a maximum and the

471 subsequent decrease at larger NO_2 mixing ratios was investigated using the kinetic box model

472 and postulated mechanism for HONO production described in Section 2.5. The aim was to

473 compare the observed production of HONO and $\gamma_{NO_2 \rightarrow HONO}$ with the modelled values, as a

474 function of NO_2 mixing ratio. The skill of the model to reproduce the observed behaviour

475 enables a validation of the postulated mechanism for HONO production, and variation of the

476 kinetic parameters enables the controlling influence of different steps in the mechanism on

477 HONO production to be evaluated.

3.3 Modelling the HONO production mechanism on illuminated TiO₂ aerosol surfaces

480 The HONO production on illuminated TiO₂ aerosol surfaces was investigated for each of the

481 mechanisms outlined in Table 1.

3.3.1 Model 1

483 Model 1 (see Table 1 and Figure 5), which contains the simplest mechanism, was designed to

484 reproduce the decreasing value of the NO_2 uptake coefficient to form HONO, $\gamma_{NO_2 \rightarrow HONO}$, with

485 increasing NO_2 and also the plateauing at higher NO_2 mixing ratios caused by NO_2 reaching a

486 maximum surface coverage, as seen by Stemmler et al., (2007). A decrease in the uptake

487 coefficient of NO_2, γ_{NO_2}, onto dust aerosol surfaces was also seen in studies where the

488 formation of HONO from NO_2 uptake was not directly studied (Ndour et al., 2008;Dupart et

489 al., 2014). The mechanism for Model 1 which is given in Table 1 describes the adsorption of

490 one NO_2 molecule to a surface site which then undergoes the reaction which forms HONO,

491 followed by desorption of HONO to the gas-phase, R9-R11. Any representation of the specific

492 chemical processes which convert NO_2 to HONO on the surface following the initial photo-

493 production of electron-hole pairs in the TiO₂ structure (R2) was not included here as the

494 primary focus was to produce the relationship between $\gamma_{NO_2 \rightarrow HONO}$ and the NO_2 mixing ratio.

495 Gustafsson et al., (2006) reported that the measured rate of photo-induced HONO production

496 is 75% that of the rate of NO_2 removal, whereas the dark disproportionation reaction (R28)

497 would predict a 50% yield, and hence that the HONO observed in their studies is not simply a

498 photo-enhancement of:

$$2NO_{2(ads)} + H_2O_{(ads)} \rightarrow HONO_{(g)} + HNO_{3(ads)} \qquad (R28)$$
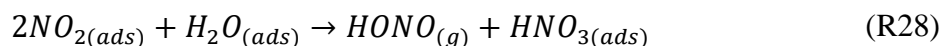
499 Gustafsson et al., (2006) suggests that an oxidant on the surface is produced following the
500 creation of the electron-hole pair (OH is generated in (R2)), and suggests H_2O_2 as a possibility,
501 which is consistent with the observation of OH and HO_2 radicals produced from the surface of
502 illuminated TiO_2 aerosols (Moon et al., 2019). For Model 1, outputs for the predicted
503 concentration of HONO and the reactive uptake coefficient, $\gamma_{NO_2 \rightarrow HONO}$, as a function of initial
504 NO_2 mixing ratio are shown in Figure 9.
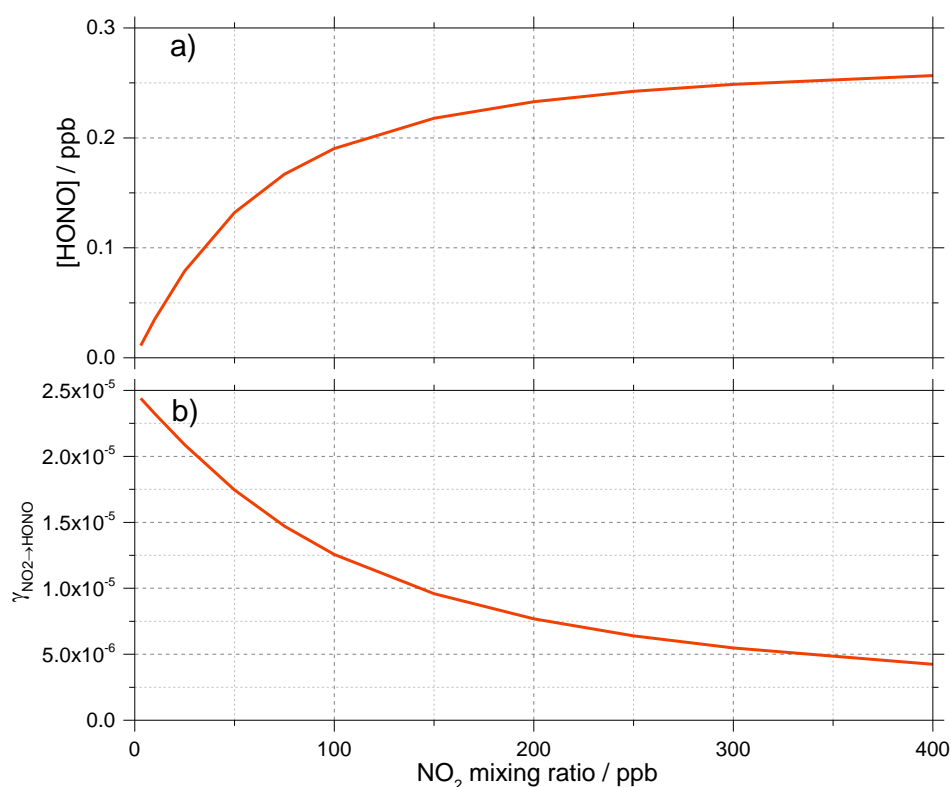
Figure 9 Model 1 calculations for (a) the concentration of HONO and (b) the reactive uptake coefficient to
form HONO, $\gamma_{NO_2 \rightarrow HONO}$, as a function of NO_2 mixing ratio for a model run time of 52 s. The estimated rate
coefficients used in this model are shown in Table 1.

505 For a run time of 52 s, equal to that of the experimental illumination time, Model 1 predicts an
506 increase in HONO production with increasing NO_2 mixing ratio until the HONO concentration
507 begins to plateau, reaching ~0.25 ppb at $[NO_2]$ = 400 ppb, presumably owing to saturation on
508 active aerosol surface sites by NO_2. This leads to the modelled reactive uptake coefficient,
509 $\gamma_{NO_2 \rightarrow HONO}$, monotonically decreasing with increasing NO_2 mixing ratio; a variation in NO_2
510 uptake coefficient similar to that seen in previous photo-enhanced NO_2 aerosol uptake studies
511 (Bröske et al., 2003;Stemmler et al., 2007;Ndour et al., 2008;Dupart et al., 2014). However,

the model predictions for Model 1 do not reproduce the experimental variations shown in Figure 6 and Figure 8, in which there is an observed initial rise and then a fall in both the HONO concentration and $\gamma_{NO_2 \rightarrow HONO}$ with increasing NO_2 mixing ratio. Hence, additional processes were considered in the model in order to try to reproduce this behaviour.

3.3.2 Models 2 and 3. Investigating the role of NO_2 dimerisation for the surface formation of HONO, and including additional surface losses of HONO

As the experimental $\gamma_{NO_2 \rightarrow HONO}$ increases with NO_2 at low NO_2 (Figure 8), we postulate in Models 2 and 3 that the production of HONO under illuminated conditions is not fully first order in NO_2 and requires more than one NO_2 molecule to form HONO, consistent with the formation of the symmetric NO_2 dimer (N_2O_4) followed by isomerisation on the surface to form the asymmetric *trans*-ONO-NO_2 dimer, which has been suggested to be more reactive with water than the symmetric N_2O_4 dimer (Finlayson-Pitts et al., 2003;Ramazan et al., 2004;Ramazan et al., 2006;Liu and Goddard, 2012) due to the autoionisation to form $(NO^+)(NO_3^-)$ which we propose is accelerated by the presence of light; the full mechanism for which is shown in Figure 5. A recent rotational spectroscopy study found that the *trans*-ONO-NO_2 was better described as the ion pair $(NO^+)(NO_3^-)$ (Seifert et al., 2017). Reaction of the $(NO^+)(NO_3^-)$ ion pair with surface adsorbed water can then lead to the formation of HONO and HNO_3, the feasibility of which is supported by molecular dynamics simulation studies (Varner et al., 2014). While the symmetric N_2O_4 dimer is favoured as it is the most stable conformer, the asymmetric forms have been experimentally observed in several studies (Fateley et al., 1959;Givan and Loewenschuss, 1989b, a, 1991;Pinnick et al., 1992;Forney et al., 1993;Wang and Koel, 1998, 1999;Beckers et al., 2010). A more recent *ab initio* study of NO_2 adsorption at the air-water interface suggested an orientational preference of NO_2 on the surface, with both oxygen atoms facing away from the interface which may imply that the asymmetric dimer ONO-NO_2 can form directly, meaning the high barrier between the symmetric and asymmetric forms does not need to be overcome (Murdachaew et al., 2013).

The energy barrier to isomerisation of symmetric N_2O_4 in the gas-phase may be reduced due to the interaction with water adsorbed on surfaces. We therefore rule out the dimer in the gas-phase adsorbing onto the surface first, and then reacting to form HONO (Varner et al., 2014). An interesting question is whether the first NO_2 molecule adsorbed to the surface dimerises via the addition of a gaseous NO_2 via an Eley-Rideal (ER) type process, or whether a Langmuir-Hinshelwood (LH) type mechanism is operating in which both NO_2 molecules are first

544   adsorbed and then diffuse together on the surface forming N_2O_4. Both ER and LH mechanisms

545   to form the NO_2 dimer have been included in the model, denoted as Model 2 and Model 3,

546   respectively. The outputs for Models 2 and 3 (see Table 1 for details of the processes included)

547   for the HONO concentration and $\gamma_{NO_2 \rightarrow HONO}$ as a function of NO_2 are shown in Figure 10

548   together with the experimental data. The stoichiometric relationship of the requirement of two

549   NO_2 molecules forming HONO on the surface was key to reproducing the experimental trend

550   of first an increase and then a decrease in both the HONO concentration and the reactive uptake

551   coefficient with the initial NO_2 mixing ratio.
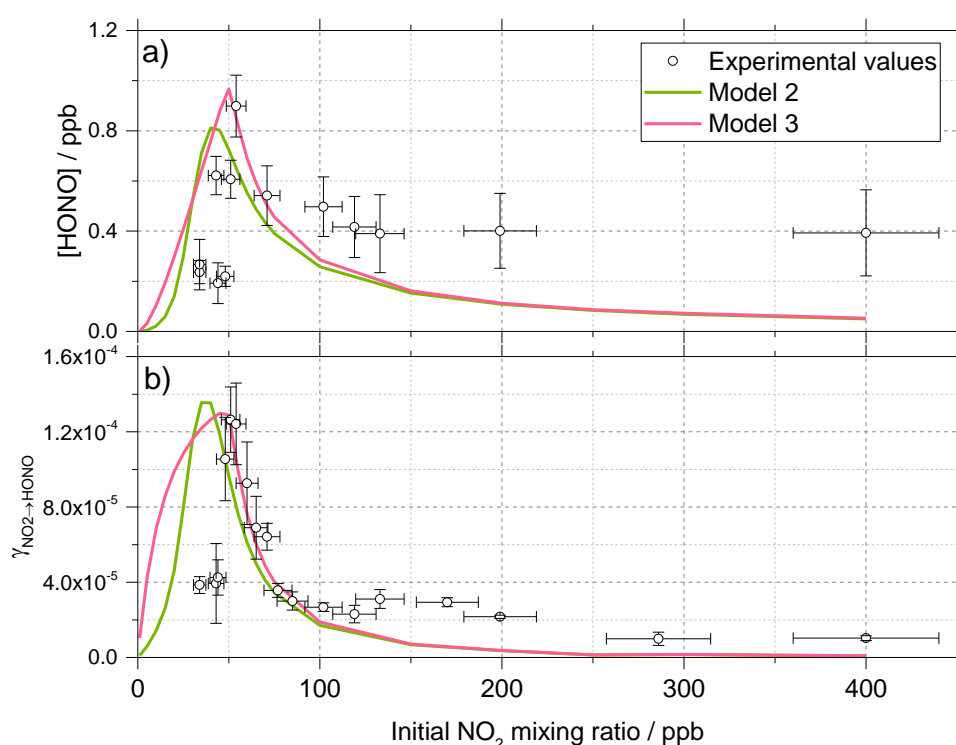
Figure 10. Experimental values (open circles with 1σ error bars), Model 2 (green line) and Model 3 (pink line) calculations for (a) HONO concentration after 52 s illumination and (b) NO_2 reactive uptake coefficient, $\gamma_{NO_2 \rightarrow HONO}$, as a function of the initial NO_2 mixing ratio. The mechanisms used for these model runs included a 2:1 stoichiometric relationship between the NO_2 adsorbed on the TiO_2 aerosol surface and the HONO produced, as well as additional HONO loss reactions which are dependent on NO_2, see Table 1 for details. Models 2 and 3 use an Eley-Rideal and Langmuir-Hinshelwood mechanisms, respectively, for the formation of the NO_2 dimer on the aerosol surface. Modelled $\gamma_{NO_2 \rightarrow HONO}$ was calculated using Eq. 6 and Eq. 7 with a constant surface area of 1.6×10^{-2} m^2m^{-3} chosen to match the aerosol surface area density of $(1.6 \pm 0.8) \times 10^{-2}$ m^2m^{-3} shown in the experimental [HONO] values in (a).

In previous work that investigated HONO production from humic acid aerosols, a saturation effect was seen with HONO production plateauing with increasing NO_2 mixing ratio (Stemmler et al., 2007), with the decreasing uptake coefficient, $\gamma_{NO_2 \rightarrow HONO}$, with increasing NO_2 being attributed to NO_2 fully saturating available surface sites. However, the observed decrease of [HONO] at the high NO_2 mixing ratios shown in Figure 8 and Figure10a suggests that additional reactions on the surface may remove HONO and result in the reduction of [HONO] that is measured. As [HONO] decreases with the increase in the NO_2 mixing ratio, the removal process should either involve NO_2 directly:

$$HONO + NO_2 \rightarrow NO + HNO_3 \qquad \text{(R19)}$$
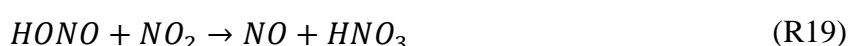
or involve species made rapidly from NO_2 on the surface, such as NO_2^+:

$$HONO_{(ads)} + NO_2^+{}_{(ads)} \rightarrow H^+ + 2NO + O_2 \qquad \text{(R19a)}$$
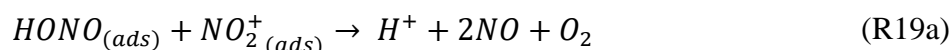
which may be present at high enough concentrations of HNO_3 on the surface (Syomin and Finlayson-Pitts, 2003) or following reaction with h_{VB}^+, or a product of the reaction of O_2^- (or e_{CB}^-) with NO_2 (R4) i.e. NO_2^-. Similar results were observed in a study by El Zein and Bedjanian (2012a) where NO_2 and NO were found to be formed from the heterogeneous reaction of HONO with TiO_2 surfaces in both dark and illuminated conditions suggesting the loss of HONO via an auto-ionisation reaction between the gas phase and adsorbed HONO to generate NO^+ and NO_2^- (El Zein and Bedjanian, 2012a). Additional HONO surface loss pathways were assumed to occur under illuminated conditions due to the presence of e^- and h^+ leading to the oxidation of HONO to NO_2 and the reduction of HONO to NO (El Zein et al., 2013). Transition state theory (TST) studies of the gas-phase reaction of HONO with NO_2 to form HNO_3 calculated a large activation energy which varied depending on whether the reaction occurs via O abstraction by HONO (159 kJ mol^{-1}) or via OH abstraction via NO_2 (~133-246 kJ mol^{-1})(Lu et al., 2000). In the gas-phase these reactions are too slow to be important but they could be enhanced on the surface, potentially more so on a photoactive surface such as TiO_2. For models 2 and 3 the shape of the trend in HONO concentration and uptake coefficient, γ, versus NO_2 concentration depended strongly on the value of k_{R19} reaction, R19, and the choice of a 2:1 stoichiometric ratio of the NO_2 molecules adsorbed to the HONO molecules produced. Without these two key processes being included, a maximum in either the HONO concentration or γ as the NO_2 concentration is increased could not be obtained in the model. A third key condition was the requirement that the desorption rate coefficient, k_{R16}, be

581 larger than the rate coefficient for the loss of HONO, k_{R17} and $k_{R18} = 1 \times 10^{-3}$ s^{-1}, but slower than

582 the adsorption rate coefficient, k_{R9}. Changing the values of all other kinetic parameters in the

583 model had an effect on the absolute concentration of HONO, but crucially not on the shape of

584 the trends in HONO or the uptake coefficient versus NO$_2$ concentration. Changing the values

585 of the rate coefficients for the gas phase loss reactions, R23-27, only had a very small impact

586 on the HONO concentration. ~~The NO$_2$ dependent loss reaction, k_{R19} in Table 1, was necessary~~

587 ~~in the model to reproduce the sharp decrease in [HONO] versus NO$_2$ seen experimentally after~~

588 ~~~54 ppb NO$_2$. Without k_{R19} the modelled [HONO] continued to increase to a plateau, as seen~~

589 ~~in Model 1 (see Figure 9). In order to observe the model output seen in Figure 10 for model 2~~

590 ~~and 3, k_{R19} also had to be slower than the desorption of HONO from the surface, k_{R16}.~~

591 The addition of an NO$_2$ dependent loss reaction to both Model 2 and 3 had the most significant

592 effect on the trend in modelled HONO concentration. Though it is also possible that a

593 secondary product could remain adsorbed and therefore block active sites on the TiO$_2$ surface,

594 effectively poisoning the photo-catalyst, NO$_2$ independent loss reactions in the model, k_{R17} and

595 k_{R18} had little effect on the trend in [HONO] vs NO$_2$, only having an effect on the overall

596 [HONO]. HNO$_3$ has however been shown to remain adsorbed to surfaces once formed

597 (Sakamaki et al., 1983;Pitts et al., 1984;Finlayson-Pitts et al., 2003;Ramazan et al., 2004) and

598 may also react with adsorbed HONO, further reducing the product yield (Finlayson-Pitts et al.,

599 2003): these NO$_2$ independent loss reactions may therefore become more important at higher

600 NO$_2$ concentrations and hence surface concentrations of HONO and HNO$_3$:

$$HONO_{(ads)} + HNO_{3(ads)} \rightarrow 2NO_{(g)} + H_2O_{(ads)} + O_{2(g)} \qquad (R17)$$
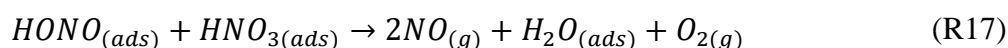
601 The photolysis of particulate nitrate was not considered in Models 2 or 3, due to the lack of

602 particulate nitrate in the system at $t = 0$. The gas-to-particle conversion of any HNO$_3$ formed

603 was not considered to be important due to the assumption that most HNO$_3$ formed would

604 remain adsorbed to the aerosol surface (Sakamaki et al., 1983;Pitts et al., 1984;Finlayson-Pitts

605 et al., 2003;Ramazan et al., 2004).

606 For Model 2, which includes the production of HONO via the Eley-Rideal mechanism, in order

607 to reproduce the experimentally observed sharp increase followed by a decrease in both

608 [HONO] and $\gamma_{NO_2 \rightarrow HONO}$ as a function of increasing NO$_2$ mixing ratio, the modelled rate

609 coefficient for the adsorption of a gas-phase NO$_2$ molecule to another the surface adsorbed

610 NO$_2$ to initially form the symmetric N$_2$O$_4$ dimer, k_{R12}, had to be larger than for the isomerisation

611 step to form HONO and HNO$_3$ via *trans*-ONO-NO$_2$, k_{R13}. Interestingly, for HONO production

via the Langmuir-Hinshelwood mechanism, Model 3, the modelled rate coefficient for the diffusion of one NO_2 molecule across the surface to form the dimer with another NO_2 molecule, k_{R14}, had to be smaller than for the isomerisation step, k_{R15}, to more closely represent the experimental results for the uptake coefficient. Additionally, in order to reproduce the experimental trend in HONO formation as a function of NO_2 mixing ratio, the rate coefficient for the NO_2 dependent loss reaction, k_{R19}, had to be larger than the NO_2 independent reactions, k_{R17} and k_{R18}, leading to $k_{R19} = 5 \times 10^{-3}$ s^{-1}. The modelled HONO concentration also sensitive to the active site surface concentration: Model 3 required an active site surface concentration 2.5 times that of Model 2 to reproduce the peak in [HONO] at ~ 51 ppb NO_2 observed in the experimental results. The reason for this is due to the difference in active site occupation in the 2 models: one active site is being occupied by two NO_2 molecules per HONO formed in Model 2 as opposed to Model 3 where two active sites are occupied per HONO formed. Regardless of the choice of an Eley Rideal or Langmuir Hinshelwood mechanism, both models reproduce the general shape of [HONO] and $\gamma_{NO_2 \rightarrow HONO}$ with NO_2, providing evidence that two NO_2 molecules are required to form HONO.

3.4 HONO production from illumination of a mixed NH_4NO_3/TiO_2 aerosol in the absence of NO_2

The photolysis of particulate nitrate has been postulated as a source of HONO under ambient sunlit conditions during several field campaigns, from both aircraft and ground based measurements (Reed et al., 2017;Ye et al., 2017a;Ye et al., 2017b). Here, experiments were carried out to investigate the formation of HONO from particulate nitrate photolysis, with and without the addition of a photo-catalyst. This is of significant interest for marine environments downwind of arid desert regions due to the availability of TiO_2 or other photocatalytic materials within aerosols in dust plumes that are transported from these regions (Hanisch and Crowley, 2003).

Using the aerosol flow tube setup described in Sections 2.1-2.4, an aqueous solution of ammonium nitrate (5 g NH_4NO_3 in 500 ml milli-Q water) was used to generate nitrate aerosols. At the RH used in this experiment, ~ 50 %, the aerosols were still deliquesced. For these experiments the residence time of the aerosols in the illuminated region of the flow tube was 30 seconds (flow rate ~ 6 lpm), with the production of HONO following illumination measured as a function of aerosol surface area density. The number of lamps was increased from 1 to 4, increasing the photon flux from $(1.63 \pm 0.09) \times 10^{16}$ to $(8.21 \pm 2.39) \times 10^{16}$ photons cm^{-2} s^{-1}

644 and $j(NO_2)$ from $(6.43 \pm 0.30) \times 10^{-3}$ to $(3.23 \pm 0.92) \times 10^{-2}$ s^{-1}. The $j(NO_2)$, $j(HONO)$ and flux

645 values for 4 lamps were more than 4 times that of 1 lamp only due to the lamp casings being

646 mirrored, and so with 4 lamps, with 2 lamps on either side of the flow tube, the casings reflected

647 the light back into the flow tube, increasing the effective light intensity. For these experiments,

648 no gaseous NO_2 was added to the gas entering the flow tube. As shown in Figure 11, for the

649 illumination of pure nitrate aerosols, although a small amount of HONO was observed at higher

650 aerosol loadings, no statistically significant production of HONO was seen.
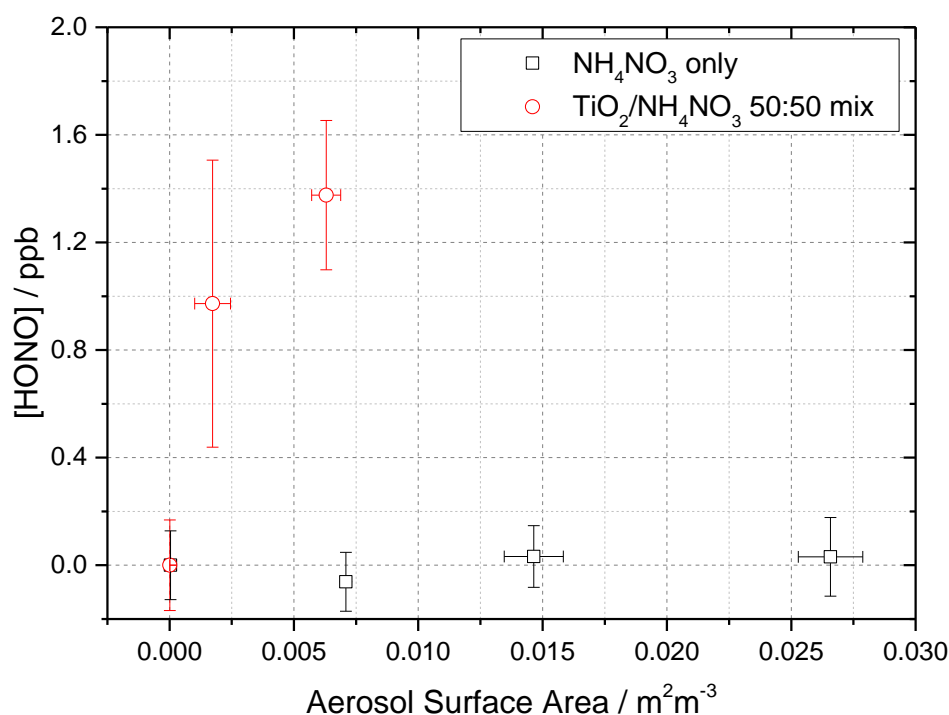
Figure 11. Dependence of the HONO concentration generated as a function of aerosol surface area density for pure NH_4NO_3 aerosol (black open squares, error bars represent 1σ) and 1:1 TiO_2/NH_4NO_3 mixed aerosol (red open circles, error bars represent 1σ). Both experiments were performed in N_2 at 295 K, an illuminated residence time of 30 s, and a lamp photon flux of $(8.29 \pm 2.39) \times 10^{16}$ photons cm^{-2} s^{-1}. The NH_4NO_3 only experiment was performed at ~50 $\pm$ 5 % RH while the TiO_2/NH_4NO_3 mix experiment was performed at 20 $\pm$ 2 % RH. For all points, the background HONO seen observed without illumination has been subtracted. At zero aerosol surface area density there is no HONO generated from the walls of the flow tube.

651 A second set of experiments were performed with an aqueous solution of titanium dioxide and

652 ammonium nitrate combined in a 1:1 mass ratio to give a TiO_2/NH_4NO_3 aerosol mixture (5 g

653 NH_4NO_3 and 5 g TiO_2 in 500 ml milli-Q water) to investigate if the photo-catalytic properties

654 of TiO_2 facilitate the production of HONO in the presence of nitrate. The RH was decreased to

655 ensure the maximum TiO_2 photocatalytic activity (Jeong et al., 2013). A recent study using

656 Raman micro spectroscopy to observe phase changes in salt particles reported an efflorescence

657   point of pure ammonium nitrate to be between 13.7-23.9 % RH (Wu et al., 2019). It is possible

658   therefore that at the RH used in this experiment, ~ 20 %, the aerosols were still deliquesced.

659   As shown in Figure 11, the presence of TiO_2 in the aerosol mixture showed a significant

660   production of HONO without the presence of NO_2, a potentially significant result for the

661   production of HONO in low NO_x environments in the presence of mixed dust/nitrate aerosols,

662   for example in oceanic regions off the coast of West Africa, or in continental regions impacted

663   by outflow from the Gobi desert. Using the Aerosol Inorganic Model (AIM) (Clegg et al.,

664   1998;Wexler and Clegg, 2002), the nitrate content of the aerosol at both 20 and 50 % RH was

665   calculated, in accordance with the experimental RH conditions. From this and the aerosol

666   volume distribution given by the SMPS, the $[NO_3^-]$ within the aerosols could be calculated.

667   The formation of HONO by photolysis of particulate nitrate is given by:

$$\frac{d[\text{HONO}]}{dt} = j(\text{pNO}_3)[\text{NO}_3^-] \tag{10}$$

668   and hence:

$$[\text{HONO}] = j(\text{pNO}_3)[\text{NO}_3^-]t \tag{11}$$

669   where $j(\text{pNO}_3)$ is the photolysis frequency of nitrate for the lamps used in these experiments

670   and t is the illumination time of the experiment. With knowledge of [HONO], $[NO_3^-]$ and $t =$

671   30 s, $j(\text{pNO}_3)$ can be calculated from a measurement of [HONO] as a function of $[NO_3^-]$, as

672   shown in Figure 12, for the mixed nitrate/ TiO_2 experiment.
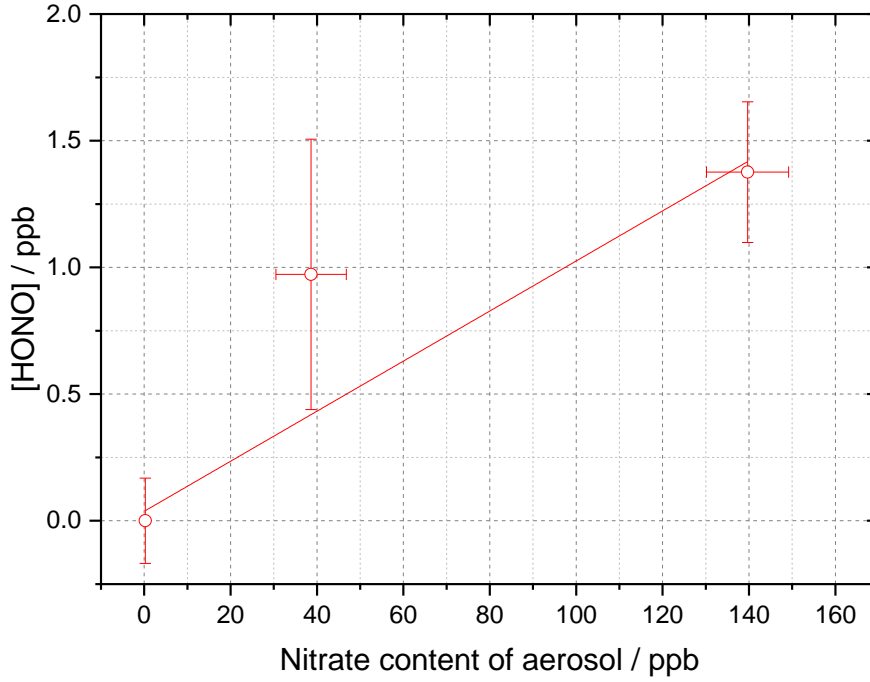
Figure 12. Dependence of [HONO] on the calculated nitrate concentration in the aerosol (using the AIM model) for the mixed TiO$_2$/ammonium nitrate aerosol experiment. Using equation 10 and for t = 30 s, the gradient gives $j(pNO_3)$ = $(3.29 \pm 0.89) \times 10^{-4}$ s^{-1}. Experiment performed at 15 ± 1 % RH, in N$_2$ at 295 K with a lamp photon flux of $(8.29 \pm 2.39) \times 10^{16}$ photons cm^{-2} s^{-1}. For all points, the background HONO seen observed without illumination has been subtracted.

673   When using the 4 lamps together, the experimental particulate nitrate photolysis rate, $j(pNO_3)$,

674   was determined to be $(3.29 \pm 0.89) \times 10^{-4}$ s^{-1} for the mixed nitrate/TiO$_2$ aerosol. From this, it

675   is possible to estimate $j(pNO_3)$ for ambient conditions typical of the tropical marine boundary

676   layer. Taking the ratio of the experimental $j(HONO)$ for 4 lamps $((8.35 \pm 0.18) \times 10^{-3}$ s^{-1}) and

677   the measured $j(HONO)$ from the RHaMBLe campaign held at the Cape Verde Atmospheric

678   Observatory [May-June,2007] $(1.2 \times 10^{-3}$ s^{-1}) (Carpenter et al., 2010;Whalley et al., 2010;Reed

679   et al., 2017) and assuming that $j(pNO_3)$ and $j(HONO)$ scale in the same way, ambient $j(pNO_3)$

680   can be determined from:

$$j(\text{pNO}_3)_N = j(\text{pNO}_3) \times \frac{1.2 \times 10^{-3}}{j(\text{HONO})} \qquad (12)$$

681   where $j(\text{pNO}_3)_N$ is the photolysis rate coefficient of particulate nitrate at Cape Verde, $j(\text{pNO}_3)$

682   is the experimentally determined photolysis rate coefficient of particulate nitrate to form

683 HONO and j(HONO) is the HONO photolysis rate coefficient calculated from the
684 experimentally determined j(NO$_2$).

685 Using j(pNO$_3$) = (3.29 ± 0.89) × 10^{-4} s^{-1}, the rate of HONO production from nitrate photolysis
686 at Cape Verde was calculated to be j(pNO$_3$)$_N$= (4.73 ± 1.01) × 10^{-5} s^{-1} from the mixed
687 nitrate/TiO$_2$ aerosol experiment. Although for pure nitrate aerosol in the absence of TiO$_2$ the
688 data were scattered and the HONO production small (Figure 11), an upper limit estimate of
689 j(pNO$_3$)$_N$=(1.06 ± 1.15) × 10^{-6} s^{-1} under conditions at Cape Verde could be made using
690 equation 11, as done for rate of HONO production from mixed nitrate/TiO$_2$ aerosols. The
691 atmospheric implications of this will be considered below.

4 Implications of HONO production from TiO$_2$ for tropospheric chemistry

4.1 Production of HONO from sunlight aerosols containing TiO$_2$ in the presence of NO$_2$

695 For the reactive uptake of NO$_2$ onto illuminated TiO$_2$ particles as a function of the initial NO$_2$
696 mixing ratio, as shown in Figure 8, a maximum value of $\gamma_{NO_2 \rightarrow HONO}$ = (1.26 ± 0.17) × 10^{-4}
697 was determined at 51 ± 5 ppb NO$_2$ for a photon flux from the lamp of (1.63 ± 0.09) × 10^{16}
698 photons cm^{-2} s^{-1}. These experiments were for single-component TiO$_2$ particles, and so for dust
699 aerosols a value of $\gamma_{NO_2 \rightarrow HONO}$ = (1.26 ± 0.17) × 10^{-5} is appropriate assuming a 10 % fraction
700 of TiO$_2$ and/or other photoactive materials (which behave similarly for HONO production) in
701 mineral dust (Hanisch and Crowley, 2003). Dust aerosols are transported from the Gobi desert
702 to urban areas of China where high NO$_x$ and nitrate aerosol concentrations have been observed
703 and in these areas HONO production facilitated by photo-catalysts may be important (Saliba
704 et al., 2014).

705 Using an average daytime maximum for [NO$_2$], j(NO$_2$) and aerosol surface area measurements
706 for a non-haze period in May-June in 2018 in Beijing, of 50 ppb, 1 × 10^{-2} s^{-1} and 2.5 × 10^{-3} m^2
707 m^{-3} (of which a maximum of 0.3 % was assumed to be TiO$_2$, though this could be higher in
708 dust impacted events (Schleicher et al., 2010)) respectively, a production rate of HONO of 1.70
709 × 10^5 molecules cm^{-3} s^{-1} (~24.8 ppt h^{-1}) has been estimated using the maximum reactive uptake
710 coefficient measured in this work, $\gamma_{NO_2 \rightarrow HONO}$ = (1.26 ± 0.17) × 10^{-4}. The average RH in
711 Beijing during summertime is significantly higher than the range of RH used in the TiO$_2$
712 aerosol experiments. In previous work (Gustafsson et al., 2006), the NO$_2$ reactive uptake
713 coefficient decreased for relative humidities above those studied here, and hence the HONO

714 The lamp

715 used to illuminate the TiO_2 aerosols in these experiments gives rise to $j(NO_2) = (6.43 \pm 0.3) \times$

716 10^{-3} s^{-1}, and so $\gamma_{NO_2 \rightarrow HONO}$ has been scaled by a factor of 1.55 to match the noon $j(NO_2)$

717 measured in May-June 2018 in Beijing (10^{-2} s^{-1}), to take into account the relatively small

718 difference in experimental and atmospheric photon flux for Beijing. The HONO production

719 rate estimated here for noontime summer [May-June 2018] in Beijing (~25 ppt hr^{-1}) is similar

720 to the value for the maximum production of HONO from urban humic acid aerosol surfaces in

721 Europe, 17 ppt h^{-1} at 20 ppb NO_2 reported by Stemmler et al., 2007. For comparison, the net

722 gaseous production rate of HONO at noon in May-June 2018 Beijing was determined from the

723 measured rate of gas-phase production and losses:

$$P_{HONO} = k_{OH+NO}[OH][NO] - (j(HONO) \times [HONO] + k_{OH+HONO}[OH][HONO]) \quad (13)$$

724 where $k_{OH+NO} = 3.3 \times 10^{-11}$ cm^3 molecule^{-1} s^{-1} (Atkinson et al., 2004), $k_{OH+HONO} = 6 \times 10^{-12}$

725 cm^3 molecule^{-1} s^{-1} (Atkinson et al., 2004) and $j(HONO)=1 \times 10^{-2}$ s^{-1} for an average maximum

726 noontime OH concentration of 8×10^6 molecules cm^{-3} (Whalley et al., 2020), NO

727 concentration of 1.45 ppb (Whalley et al., 2020) and HONO concentration of 0.8 ppb (Whalley

728 et al., 2020).

729 The net gas-phase production of HONO from equation 13 was calculated to be -3.8 ppb hr^{-1} (a

730 net loss) as expected due to HONO loss by photolysis peaking at solar noon, suggesting the

731 production of HONO heterogeneously from TiO_2 and NO_2 (~25 ppt hr^{-1}) would have little

732 effect on the overall HONO budget for Beijing summertime at noon.

733 ## 4.2 Production of HONO from photolysis of mixed dust/nitrate aerosols

734 Oceanic environments, for example the Atlantic Ocean which is impacted by both dust aerosols

735 from the Sahara and high concentrations of mixed nitrate aerosols from sea spray, and despite

736 low NO_2 concentrations could be important for particulate nitrate photolysis as a source of

737 HONO (Hanisch and Crowley, 2003;Ye et al., 2017b). From the particulate nitrate photolysis

738 experiments in the absence of NO_2 conducted here, a $j(pNO_3)_N = (4.73 \pm 1.01) \times 10^{-5}$ s^{-1} was

739 determined in the presence of the TiO_2 photo-catalysts (Section 3.4). Using the experimental

740 $j(pNO_3)$, scaled to typical ambient light levels, and a mean noon concentration of nitrate

741 aerosols of 400 ppt measured at Cape Verde (Reed et al., 2017), taken as an example marine

742 boundary layer environment with a high concentration of mineral dust aerosols, a rate of

743 HONO production from particulate nitrate at Cape Verde was calculated as 4.65×10^5

744   molecule cm^{-3} s^{-1} (68 ppt hr^{-1}). We note that this value would be ~ 50 times smaller for pure

745   nitrate aerosols. The missing rate of HONO production i.e. not taken into account by the gas

746   phase production and loss, P_{other}, from the Cape Verde RHaMBLe campaign, can be calculated

747   using the observed HONO concentration, [HONO] and the known gas-phase routes for HONO

748   production and loss:

$$P_{other} = ([HONO](j(HONO) + k_{OH+HONO}[OH])) - (k_{OH+NO}[OH][NO])) \qquad (14)$$

749   where $k_{OH+NO} = 3.3 \times 10^{-11}$ cm^3 molecule^{-1} s^{-1} (Atkinson et al., 2004), $k_{OH+HONO} = 6 \times 10^{-12}$

750   cm^3 molecule^{-1} s^{-1} (Atkinson et al., 2004) and $j(HONO)=2 \times 10^{-3}$ s^{-1} for average maximum

751   measured concentrations of 1×10^7 molecules cm^{-3} for OH (Whalley et al., 2010), 5.41×10^7

752   molecule cm^{-3} for NO (Whalley et al., 2010) and 1.23×10^8 molecule cm^{-3} for HONO (Whalley

753   et al., 2010).

754   Using equation 14 this missing HONO production rate for Cape Verde was 34.6 ppt hr^{-1}, which

755   is within a factor of two of the rate of HONO production (68 ppt hr-1) calculated from nitrate

756   photolysis using our experimental HONO production data for mixed nitrate/TiO$_2$ aerosols.

757   These results provide further evidence that particulate nitrate photolysis in the presence of

758   photocatalytic compounds such as TiO$_2$ found in dust could be significant in closing the HONO

759   budget for this environment (Whalley et al., 2010;Reed et al., 2017;Ye et al., 2017a).

5   Conclusions.

761   The experimental production of HONO from both illuminated TiO$_2$ aerosols in the presence of

762   NO$_2$ and from mixed nitrate/TiO$_2$ aerosols in the absence of NO$_2$ was observed, with the

763   HONO concentrations measured using photo-fragmentation laser-induced fluorescence

764   spectroscopy. Using experimental data, the reactive uptake of NO$_2$ onto the TiO$_2$ aerosol

765   surface to produce HONO, $\gamma_{NO_2 \rightarrow HONO}$, was determined for NO$_2$ mixing ratios ranging from

766   34 to 400 ppb, with a maximum $\gamma_{NO_2 \rightarrow HONO}$ value of $(1.26 \pm 0.17) \times 10^{-4}$ for single-component

767   TiO$_2$ aerosols observed at 51 ppb NO$_2$, and for a lamp photon flux of $(1.65 \pm 0.02) \times 10^{16}$

768   photons cm^{-2} s^{-1} (integrated between 290 and 400 nm). The measured reactive uptake

769   coefficient, $\gamma_{NO_2 \rightarrow HONO}$, showed an increase then subsequent decrease as a function of NO$_2$

770   mixing ratio, peaking at 51 ± 5 ppb. Box modelling studies supported a mechanism involving

771   two NO$_2$ molecules on the aerosol surface per HONO molecule generated, providing evidence

772   for the formation of a surface-bound NO$_2$ dimer intermediate. The exact mechanism for HONO

773   formation, for examples the step(s) which are accelerated in the presence of light, remains

774   unclear, although previous studies would suggest the process occurs via the isomerisation of

the symmetric N_2O_4 dimer to give *trans*-ONO-NO_2, either via *cis*-ONO-NO_2 or directly, suggested to be more reactive with water than the symmetric dimer (Finlayson-Pitts et al., 2003;Ramazan et al., 2004;Ramazan et al., 2006;de Jesus Madeiros and Pimentel, 2011;Liu and Goddard, 2012;Murdachaew et al., 2013;Varner et al., 2014). Investigations into the RH dependence of the HONO production mechanism on TiO_2 aerosols showed a peak in production between ~25-30 % RH, with lower HONO production at higher NO_2 mixing ratios observed for all RHs tested. The increase in HONO production with increasing RH can be attributed to a higher concentration of H_2O on the surface increasing its availability for the hydrolysis reaction to give HONO, whereas a decrease in HONO production after RH ~ 30 % could be due to the increased water surface concentration inhibiting the adsorption of NO_2. Using the laboratory reactive uptake coefficient for HONO production, $\gamma_{NO_2 \rightarrow HONO}$, the rate of production of HONO from illuminated aerosols in Beijing in summer for typical NO_2 mixing ratios and aerosol surface areas was found to be similar to that estimated previously for the production of HONO from urban humic acid aerosol surfaces in Europe.

In the absence of NO_2, significant HONO production from 50:50 mixed nitrate/TiO_2 aerosols was measured. Using the experimental HONO concentrations observed, a rate of HONO production from nitrate photolysis was calculated, which was then scaled to the ambient conditions encountered at the Cape Verde Atmospheric Observatory in the tropical marine boundary layer. A HONO production rate of 68 ppt hr^{-1} for the mixed nitrate/TiO_2 aerosol was found for CVAO conditions, similar in magnitude to the missing HONO production rate that had been calculated previously in order to bring modelled HONO concentrations into line with field-measured values at CVAO. These results provide further evidence that aerosol particulate nitrate photolysis may be significant as a source of HONO, and hence NO_x, in the remote marine boundary layer, where mixed aerosols containing nitrate and a photo-catalytic species such as TiO_2, as found in dust, are present.

However, the production of HONO from pure, deliquesced ammonium nitrate aerosols alone could not be definitively confirmed over the range of conditions used in our experiments, suggesting that another component within the aerosol is necessary for HONO production. Future work should be directed towards studying pure nitrate aerosols over a wider range of conditions, for example varying the aerosol pH, and also adding other chemical species into the aerosol which may promote HONO production.

Data availability. Data presented in this study can be obtained from authors upon request (d.e.heard@leeds.ac.uk)

808 *Competing interests.* The authors declare that they have no conflict of interest.

809 *Acknowledgements.* We are grateful to the Natural Environmental Research Council for
810 funding a SPHERES PhD studentship (Joanna E. Dyson) and for funding the EXHALE project
811 (grant number NE/S006680/1).

References

813 Alicke, B., Platt, U., and Stutz, J.: Impact of nitrous acid photolysis on the total hydroxyl radical
814 budget during the Limitation of Oxidant Production/Pianura Padana Produzione di Ozono
815 study in Milan, J. Geophys. Res. Atmos., 107, https://doi.org/10.1029/2000JD000075, 2002.

816 Atkinson, R., Baulch, D. L., Cox, R. A., Crowley, J. N., Hampson, R. F., Hynes, R. G., Jenkin,
817 M. E., Rossi, M. J., and Troe, J.: Evaluated kinetic and photochemical data for atmospheric
818 chemistry: Volume I - gas phase reactions of O_x, HO_x, NO_x and SO_x species, Atmos. Chem.
819 Phys., 4, 1461-1738, https://doi.org/10.5194/acp-4-1461-2004, 2004.

820 Beckers, H., Zeng, X., and Willner, H.: Intermediates involved in the oxidation of nitrogen
821 monoxide: Photochemistry of the cis-$N_2O_2 \cdot O_2$ complex and of sym-N_2O_4 in Solid Ne Matrices,
822 Chemistry–A European Journal, 16, 1506-1520, https://doi.org/10.1002/chem.200902406,
823 2010.

824 Bedjanian, Y., and El Zein, A.: Interaction of NO_2 with TiO_2 Surface Under UV Irradiation:
825 Products Study, J. Phys. Chem. A, 116, 1758-1764, https://doi.org/10.1021/jp210078b, 2012.

826 Boustead, G. A.: Measurement of nitrous acid production from aerosol surfaces using Photo-
827 Fragmentation Laser-Induced Fluorescence, School of Chemistry, University of Leeds, 2019.

828 Bröske, R., Kleffmann, J., and Wiesen, P.: Heterogeneous conversion of NO_2 on secondary
829 organic aerosol surfaces: A possible source of nitrous acid (HONO) in the atmosphere?, Atmos.
830 Chem. Phys., 3, 469-474, https://doi.org/10.5194/acp-3-469-2003, 2003.

831 Cantrell, C., Zimmer, A., and Tyndall, G. S.: Adsorption cross sections for water vapor from
832 183 to 193 nm, Geophys. Res. Lett., 24, 2195-2198, https://doi.org/10.1029/97GL02100, 1997.

833 Carpenter, L. J., Fleming, Z. L., Read, K. A., Lee, J. D., Moller, S. J., Hopkins, J. R., Purvis,
834 R. M., Lewis, A. C., Müller, K., Heinold, B., Herrmann, H., Fomba, K. W., van Pinxteren, D.,
835 Müller, C., Tegen, I., Wiedensohler, A., Müller, T., Niedermeier, N., Achterberg, E. P., Patey,
836 M. D., Kozlova, E. A., Heimann, M., Heard, D. E., Plane, J. M. C., Mahajan, A., Oetjen, H.,
837 Ingham, T., Stone, D., Whalley, L. K., Evans, M. J., Pilling, M. J., Leigh, R. J., Monks, P. S.,
838 Karunaharan, A., Vaughan, S., Arnold, S. R., Tschritter, J., Pöhler, D., Frieß, U., Holla, R.,
839 Mendes, L. M., Lopez, H., Faria, B., Manning, A. J., and Wallace, D. W. R.: Seasonal
840 characteristics of tropical marine boundary layer air measured at the Cape Verde Atmospheric
841 Observatory, Journal of Atmospheric Chemistry, 67, 87-140, https://doi.org/10.1007/s10874-
842 011-9206-1, 2010.

843 Chen, H., Nanayakkara, C. E., and Grassian, V. H.: Titanium dioxide photocatalysis in
844 atmospheric chemistry, Chem. Rev., 112, 5919-5948, https://doi.org/10.1021/cr3002092,
845 2012.

846 Clegg, S. L., Brimblecombe, P., and Wexler, A. S.: Thermodynamic model of the system H^+-
847 $NH_4^+- Na^+- SO_4^{2-} NO_3^-- Cl^- H_2O$ at 298.15 K, J. Phys. Chem. A, 102, 2155-2171,
848 https://doi.org/10.1021/jp973043j, 1998.

849 Crilley, L. R., Kramer, L. J., Ouyang, B., Duan, J., Zhang, W., Tong, S., Ge, M., Tang, K., Qin,
850 M., Xie, P., Shaw, M. D., Lewis, A. C., Mehra, A., Bannan, T. J., Worrall, S. D., Priestley, M.,
851 Bacak, A., Coe, H., Allan, J., Percival, C. J., Popoola, O. A. M., Jones, R. L., and Bloss, W. J.:
852 Intercomparison of nitrous acid (HONO) measurement techniques in a megacity (Beijing),
853 Atmos. Meas. Tech., 12, 6449-6463, https://doi.org/10.5194/amt-12-6449-2019, 2019.

854 de Jesus Madeiros, D., and Pimentel, A. S.: New insights in the atmospheric HONO formation:
855 new pathways for N_2O_4 isomerisaton and NO_2 dimerisation in the presence of water. , J. Phys.
856 Chem. A, 115, 6357-6365, https://doi.org/10.1021/jp1123585, 2011.

857 Dupart, Y., Fine, L., D'Anna, B., and George, C.: Heterogeneous uptake of NO_2 on Arizona
858 Test Dust under UV-A irradiation: an aerosol flow tube study, Aeolian Res., 15, 45-51,
859 https://doi.org/10.1016/j.aeolia.2013.10.001, 2014.

860 El Zein, A., and Bedjanian, Y.: Reactive Uptake of HONO to TiO_2 Surface: "Dark" Reaction,
861 J. Phys. Chem. A, 116, 3665-3672, https://doi.org/10.1021/jp300859w, 2012a.

862 El Zein, A., and Bedjanian, Y.: Interaction of NO_2 with TiO_2 surface under UV irradiation:
863 measurements of uptake coefficient, Atmos. Chem. Phys., 12, 1013-1020,
864 https://doi.org/10.5194/acp-12-1013-2012, 2012b.

865 El Zein, A., Bedjanian, Y., and Romanias, M. N.: Kinetics and products of HONO interaction
866 with TiO_2 surface under UV irradiation, Atmos. Environ., 67, 203-210,
867 https://doi.org/10.1016/j.atmosenv.2012.11.016, 2013.

868 Fateley, W. G., Bent, H. A., and Crawford Jr, B.: Infrared spectra of the frozen oxides of
869 nitrogen, J. Chem. Phys., 31, 204-217, https://doi.org/10.1063/1.1730296, 1959.

870 Finlayson-Pitts, B. J., Wingen, L. M., Summer, A. L., Syomin, D., and Ramazan, K. A.: The
871 heterogeneous hydrolysis of NO_2 in laboratory systems in outdoor and indoor atmospheres: An
872 intergrated mechanism, Phys.Chem.Phys.Chem, 5, 223-242, https://doi.org/10.1039/b208564j,
873 2003.

874 Forney, D., Thompson, W. E., and Jacox, M. E.: The vibrational spectra of molecular ions
875 isolated in solid neon. XI. NO_2^+, NO_2^-, and NO_3^-, The Journal of Chemical Physics, 99, 7393-
876 7403, https://doi.org/10.1063/1.465720, 1993.

877 Gandolfo, A., Bartolomei, V., Gomez Alvarez, E., Tlili, S., Gligorovski, S., Kleffmann, J., and
878 Wortham, H.: The effectiveness of indoor photocatalytic paints on NOx and HONO levels,
879 Applied Catalysis B: Environmental, 166-167, 84-90,
880 https://doi.org/10.1016/j.apcatb.2014.11.011, 2015.

881 Gandolfo, A., Rouyer, L., Wortham, H., and Gligorovski, S.: The influence of wall temperature
882 on NO2 removal and HONO levels released by indoor photocatalytic paints, Applied Catalysis
883 B: Environmental, 209, 429-436, https://doi.org/10.1016/j.apcatb.2017.03.021, 2017.

884 George, C., Strekowski, R. S., Kleffmann, J., Stemmler, K., and Ammann, M.: Photoenhanced
885 uptake of gaseous NO_2 on solid organic compounds: a photochemical source of HONO?,
886 Faraday Discuss., 130, https://doi.org/10.1039/b417888m, 2005.

887 George, I. J., Matthews, P. S. J., Whalley, L. K., Brooks, B., Goddard, A., Baeza-Romero, M.,
888 and Heard, D. E.: Measurements of uptake coefficients for heterogeneous loss of HO_2 onto
889 submicron inorganic salt aerosols., Phys. Chem. Chem. Phys., 15, 12829-12845,
890 https://doi.org/10.1039/c3cp51831k, 2013.

891 Ginoux, P., Chin, M., Tegen, I., Prospero, J. M., Holben, B., Dubovik, O., and Lin, S. J.:
892 Sources and distributions of dust aerosols simulated with the GOCART model, J. Geophys.
893 Res. Atmos., 106, 20255-20273, https://doi.org/10.1029/2000JD000053, 2001.

894 Givan, A., and Loewenschuss, A.: Fourier transform infrared and Raman studies on solid
895 nitrogen dioxide: Temperature cycling of ordered, disordered, and multicomponent layers, The
896 Journal of Chemical Physics, 90, 6135-6142, https://doi.org/10.1063/1.456379, 1989a.

897 Givan, A., and Loewenschuss, A.: On the intermolecularity or intramolecularity of nitrosonium
898 nitrate formation in thin films of nitrogen dioxide: A Fourier transform infrared study, The
899 Journal of chemical physics, 91, 5126-5127, https://doi.org/10.1063/1.457609, 1989b.

900 Givan, A., and Loewenschuss, A.: Fourier transform infrared study of amorphous N_2O_4 solid:
901 Destabilization with inert impurities, The Journal of chemical physics, 94, 7562-7563,
902 https://doi.org/10.1063/1.460192, 1991.

903 Goodman, A. L., Bernard, E. T., and Grassian, V. H.: Spectroscopic study of nitric acid and
904 water adsorption on oxide particles: enhanced nitric acid uptake kinetics in the presence of
905 adsorbed water, J. Phys. Chem. A, 105, 6443-6457, https://doi.org/10.1021/jp0037221, 2001.

906 Gustafsson, R. J., Orlov, A., Griffiths, P. T., Cox, R. A., and Lambert, R. M.: Reduction of
907 NO_2 to nitrous acid on illuminated titanium dioxide aerosol surfaces: implications for
908 photocatalysis and atmospheric chemistry, Chem. Commun., 37, 3936-3938,
909 https://doi.org/10.1039/b609005b, 2006.

910 Hanisch, F., and Crowley, J. N.: Ozone decomposition on Saharan dust: an experimental
911 investigation, Atmos. Chem. Phys., 3, 119-130, https://doi.org/10.5194/acp-3-119-2003, 2003.

912 Harrison, R. M., Peak, J. D., and Collins, G. M.: Tropospheric cycle of nitrous acid, J. Geophys.
913 Res. Atmos., 101, 14429-14439, https://doi.org/10.1029/96JD00341, 1996.

914 Heard, D. E.: Atmospheric field measurements of the hydroxyl radical using Laser-Induced
915 Fluorescence spectroscopy, Annu. Rev. Phys. Chem., 57, 191-216,
916 https://doi.org/10.1146/annurev.physchem.57.032905.104516, 2006.

917 Jeong, M.-G., Park, E. J., Seo, H. O., Kim, K.-D., Kim, Y. D., and Lim, D. C.: Humidity effect
918 on photocatalytic activity of TiO_2 and regeneration of deactivated photocatalysts, Appl. Surf.
919 Sci., 271, 164-170, https://doi.org/10.1016/j.apsusc.2013.01.155, 2013.

920 Kleffmann, J.: Daytime sources of nitrous acid (HONO) in the atmospheric boundary layer,
921 Chem. Phys. Chem., 8, 1137-1144, https://doi.org/10.1002/cphc.200700016, 2007.

922 Kurtenbach, R., Becker, K. H., Gomes, J. A. G., Kleffmann, J., Lörzer, J. C., Spittler, M.,
923 Wiesen, P., Ackermann, R., Geyer, A., and Platt, U.: Investigations of emissions and
924 heterogeneous formation of HONO in road traffic tunnel, Atmos. Environ., 35, 3385-3394,
925 https://doi.org/10.1016/S1352-2310(0)00138-8, 2001.

926 Langridge, J. M., Gustafsson, R. J., Griffiths, P. T., Cox, R. A., Lambert, R. M., and Jones, R.
927 L.: Solar driven nitrous acid formation on building material surfaces containing titanium
928 dioxide: A concern for air quality in urban areas?, Atmos. Environ., 43, 5128-5131,
929 https://doi.org/10.1016/j.atmosenv.2009.06.046, 2009.

930 Lee, J. D., Whalley, L. K., Heard, D. E., Stone, D., Dunmore, R. E., Hamilton, J. F., Young,
931 D. E., Allan, J. D., Laufs, S., and Kleffmann, J.: Detailed budget analysis of HONO in central
932 London reveals a missing daytime source, Atmos. Chem. Phys., 16, 2747-2764,
933 https://doi.org/10.5194/acp-16-2747-2016, 2016.

934 Levy, H.: Normal atmosphere: large radical and formaldehyde concentrations predicted,
935 Science, 173, 141-143, https://doi.org/10.1126/science.173.3992.141, 1971.

936 Li, S., Matthews, J., and Sinha, A.: Atmospheric hydroxyl radical production from
937 electronically excited NO_2 and H_2O, Science, 319, https://doi.org/10.1126/science.1151443,
938 2008.

939 Liao, W., Hecobian, A., Mastromarino, J., and Tan, D.: Development of a photo-
940 fragmentation/laser-induced fluorescence measurement of atmospheric nitrous acid, Atmos.
941 Environ., 40, 17-26, https://doi.org/10.1016/j.atmosenv.2005.07.001, 2006.

942 Liao, W., Hecobian, A., Mastromarino, J., and Tan, D.: Development of a photo-
943 fragmentation/laser-induced fluorescence measurement of atmospheric nitrous acid,
944 Atmospheric Envrionment, 40, 17-26, https://doi.org/10.1016/j.atmosenv.2005.07.001, 2007.

945 Liu, W. G., and Goddard, W. A.: First-principle study of the role of interconversion between
946 NO_2, N_2O_4, *cis*-ONO-NO_2, and *trans*-ONO-NO_2 in chemical processes, J. Am. Chem. Soc.,
947 134, 12970-12978, https://doi.org/10.1021/ja300545e, 2012.

948 Lu, K., Fuchs, H., Hofzumahaus, A., Tan, Z., Wang, H., Zhang, L., Schmitt, S. H., Rohrer, F.,
949 Bohn, B., Broch, S., Dong, H., Gkatzelis, G. I., Hohaus, T., Holland, F., Li, X., Liu, Y., Liu,
950 Y., Ma, X., Novelli, A., Schlag, P., Shao, M., Wu, Y., Wu, Z., Zeng, L., Hu, M., Kiendler-
951 Scharr, A., Wahner, A., and Zhang, Y.: Fast Photochemistry in Wintertime Haze:
952 Consequences for Pollution Mitigation Strategies, Environ. Sci. Technol., 53, 10676-10684,
953 https://doi.org/10.1021/acs.est.9b02422, 2019.

954 Lu, X., Park, J., and Lin, M. C.: Gas phase reactions of HONO with NO_2, O_3 and HCl: Ab initio
955 and TST study, J. Phys. Chem. A, 104, 8730-8738, https://doi.org/10.1021/jp001610o, 2000.

956 Matthews, P. S. J., Baeza-Romero, M. T., Whalley, L. K., and Heard, D. E.: Uptake of HO_2
957 radicals onto Arizona test dust particles using an aerosol flow tube, Atmos. Chem. Phys., 14,
958 7397-7408, https://doi.org/10.5194/acp-14-7397-2014, 2014.

959 MCPA software Ltd.: Facsimile, 2020.

960 Michoud, V., Colomb, A., Borbon, A., Miet, K., Beekmann, M., Camredon, M., Aumont, B.,
961 Perrier, S., Zapf, P., Siour, G., Ait-Helal, W., Afif, C., Kukui, A., Furger, M., Dupont, J. C.,
962 Haeffelin, M., and Doussin, J. F.: Study of the unknown HONO daytime source at a European
963 suburban site during the MEGAPOLI summer and winter field campaigns, Atmos. Chem.
964 Phys., 14, 2805-2822, https://doi.org/10.5194/acp-14-2805-2014, 2014.

965 Moon, D. R., Ingham, T., Whalley, L. K., Seakins, P. W., Baeza-Romero, M. T., and Heard,
966 D. E.: Production of OH and HO_2 radicals from near-UV irradiated airborne TiO_2
967 nanoparticles, Phys.Chem.Phys.Chem, 21, 2325-2336, https://doi.org/10.1039/C8CP06889E,
968 2019.

969 Murdachaew, G., Varner, M. E., Philips, L. F., Finlayson-Pitts, B. J., and Gerber, R. B.:
970 Nitrogen dioxide at the air-water interface: trapping, adsorption, and solvation in the bulk and
971 at the surface, Phys. Chem. Chem. Phys., 15, 204-212, https://doi.org/10.1039/c2cp42810e,
972 2013.

973 Nakamura, I., Sugihara, S., and Takeuchi, K.: Mechanism for NO photooxidation over the
974 oxygen-deficient TiO_2 powder under visible light irradiation, Chem. Lett., 29, 1276-1277,
975 https://doi.org/10.1246/cl.2000.1276, 2000.

976 Ndour, M., D'Anna, B., George, C., Ka, O., Balkanski, Y., Kleffman, J., Stemmler, K., and
977 Ammann, M.: Photoenhanced uptake of NO_2 on mineral dust: Laboratory experiments and

978   model simulations, Geophys. Res. Lett., 35, L05812, https://doi.org/10.1029/2007GL032006,
979   2008.

980   Oswald, R., Behrendt, T., Ermel, M., Wu, D., Su, H., Cheng, Y., Breuninger, C., Moravek, A.,
981   Mougin, E., Delon, C., Loubet, B., Pommerening-Röser, A., Sörgel, M., Pöschl, U., Hoffmann,
982   T., Andeae, M. O., Meixner, F. X., and Trebs, I.: HONO emissions from soil bacteria as a
983   major   source   of   atmospheric   reactive   nitrogen,   Science,   341,   1233-1235,
984   https://doi.org/10.1126/science.1242266, 2013.

985   Pinnick, D., Agnew, S., and Swanson, B.: Fluid dinitrogen tetroxide at very high pressure and
986   high temperature: observation of the nitrite isomer, The Journal of Physical Chemistry, 96,
987   7092-7096, https://doi.org/10.1021/j100196a046, 1992.

988   Pitts, J. N., Sanhueza, E., Atkinson, R., Carter, W. P. L., Winer, A. M., Harris, G. W., and
989   Plum, C. N.: An investigation of the dark formation of nitrous acid in environmental chambers,
990   Int. J. Chem. Kinet., 16, 919-939, https://doi.org/10.1002/kin.550160712, 1984.

991   Platt, U., Perner, D., Harris, G. W., Winer, A. M., and Pitts, J. N.: Observations of nitrous acid
992   in an urban atmosphere by differential optical absorption, Nature, 285, 312-314,
993   https://doi.org/10.1038/285312a0, 1980.

994   Ramazan, K. A., Syomin, D., and Finlayson-Pitts, B. J.: The photochemical production of
995   HONO during the heterogeneous hydrolysis of NO2, Phys. Chem. Chem. Phys., 6, 3836-3843,
996   https://doi.org/10.1039/B402195A, 2004.

997   Ramazan, K. A., Wingen, L. M., Miller, Y., Chaban, G. M., Gerber, R. B., Xantheas, S. S., and
998   Finlayson-Pitts, B. J.: New experimental and theoretical approach to the heterogeneous
999   hydrolysis of NO_2: key role of molecular nitric acid and its complexes, J. Phys. Chem. A, 110,
1000   6886-6897, https://doi.org/10.1021/jp056426n, 2006.

1001   Reed, C., Evans, M. J., Crilley, L. R., Bloss, W. J., Sherwen, T., Read, K. A., Lee, J. D., and
1002   Carpenter, L. J.: Evidence for renoxification in the tropical marine boundary layer, Atmos.
1003   Chem. Phys., 17, 4081-4092, https://doi.org/10.5194/acp-17-4081-2017, 2017.

1004   Sakamaki, F., Hatakeyama, S., and Akimoto, H.: Formation of nitrous acid and nitric oxide in
1005   the heterogeneous dark reaction of nitrogen dioxide and water vapor in a smog chamber, Int.
1006   J. Chem. Kinet., 15, 1013-1029, https://doi.org/10.1002/kin.550151006, 1983.

1007   Saliba, N., Moussa, S., and Tayyar, G.: Contribution of airborne dust particles to HONO
1008   sources, Atmos. Chem. Phys. Discuss., 14, https://doi.org/10.5194/acpd-14-4827-2014, 2014.

1009   Sander, S., Friedl, R., Barker, J., Golden, D., Kurylo, M., Wine, P., Abbatt, J., Burkholder, J.,
1010   Kolb, C., and Moortgat, G.: Chemical kinetics and photochemical data for use in atmospheric
1011   studies, evaluation number 14, JPL Publ., 02, 25, 2003.

1012   Schleicher, N., Norra, S., Chai, F., Chen, Y., Wang, S., and Stüben, D.: Anthropogenic versus
1013   geogenic contribution to total suspended atmospheric particulate matter and its variations
1014   during a two-year sampling period in Beijing, China, J. Environ. Monit., 12, 434-441,
1015   https://doi.org/10.1039/B914739J, 2010.

1016   Seifert, N. A., Zaleski, D. P., Fehnel, R., Goswami, M., Pate, B. H., Lehmann, K. K., Leung,
1017   H. O., Marshall, M. D., and Stanton, J. F.: The gas-phase structure of the asymmetric, trans-
1018   dinitrogen tetroxide (N_2O_4), formed by dimerization of nitrogen dioxide (NO_2), from rotational
1019   spectroscopy and ab initio quantum chemistry, The Journal of Chemical Physics, 146, 134305,
1020   https://doi.org/10.1063/1.4979182, 2017.

Shan, J. H., Wategaonkar, S. J., and Vasudev, R.: Vibrational state dependence of the A state lifetime of HONO, Chem. Phys. Lett., 158, 317-320, https://doi.org/10.1016/0009-2614(89)87343-9, 1989.

Slater, E. J., Whalley, L. K., Woodward-Massey, R., Ye, C., Lee, J. D., Squires, F., Hopkins, J. R., Dunmore, R. E., Shaw, M., Hamilton, J. F., Lewis, A. C., Crilley, L. R., Kramer, L., Bloss, W., Vu, T., Sun, Y., Xu, W., Yue, S., Ren, L., Acton, W. J. F., Hewitt, C. N., Wang, X., Fu, P., and Heard, D. E.: Elevated levels of OH observed in haze events during wintertime in central Beijing, Atmos. Chem. Phys. Discuss., 2020, 1-43, https://doi.org/10.5194/acp-2020-362, 2020.

Spataro, F., and Ianniello, A.: Sources of atmospheric nitrous acid: State of the science, current research needs, and future prospects, J. Air Waste Manage. Assoc., 64, 1232-1250, https://doi.org/10.1080/10962247.2014.952846, 2014.

Stemmler, K., Ndour, M., Elshorbany, Y., Kleffmann, J., D'Anna, B., George, C., Bohn, B., and Ammann, M.: Light induced conversion of nitrogen dioxide into nitrous acid on submicron humic acid aerosol, Atmos. Chem. Phys., 7, 4237-4248, https://doi.org/10.5194/acp-7-4237-2007, 2007.

Su, H., Cheng, Y., Oswald, R., Behrendt, T., Trebs, I., Meixner, F. C., Andreae, M. O., Cheng, P., Zhang, Y., and Pöschl, U.: Soil nitrate as a source of atmospheric HONO and OH radicals, Science, 333, 1616-1618, https://doi.org/10.1126/science.1207687, 2011.

Syomin, D. A., and Finlayson-Pitts, B. J.: HONO decomposition on borosilicate glass surfaces: implications for environmental chamber studies and field experiments, Phys. Chem. Chem. Phys., 5, 5236-5242, https://doi.org/10.1039/b309851f, 2003.

Takeuchi, M., Sakamoto, K., Martra, G., Coluccia, S., and Anpo, M.: Mechanism of photoinduced superhydrophilicity on the TiO_2 photocatalyst surface, J. Phys. Chem. B, 109, 15422-15428, https://doi.org/10.1021/jp058075i, 2005.

Varner, M. E., Finlayson-Pitts, B. J., and Gerber, R. B.: Reaction of a charge-separated $ONONO_2$ species with water in the formation of HONO: an MP2 molecular dynamics study, Phys. Chem. Chem. Phys., 16, 4483-4487, https://doi.org/10.1039/c3cp55024a, 2014.

Wang, C., Bottorff, B., Reidy, E., Rosales, C. M. F., Collins, D. B., Novoselac, A., Farmer, D. K., Vance, M. E., Stevens, P. S., and Abbatt, J. P. D.: Cooking, Bleach Cleaning, and Air Conditioning Strongly Impact Levels of HONO in a House, Environ. Sci. Technol., 54, 13488-13497, 10.1021/acs.est.0c05356, 2020.

Wang, J., and Koel, B. E.: IRAS studies of NO_2, N_2O_3, and N_2O_4 adsorbed on Au (111) surfaces and reactions with coadsorbed H_2O, J. Phys. Chem. A, 102, 8573-8579, https://doi.org/10.1021/jp982061d, 1998.

Wang, J., and Koel, B. E.: Reactions of N_2O_4 with ice at low temperatures on the Au (111) surface, Surf. Sci., 436, 15-28, https://doi.org/10.1016/S0039-6028(99)00457-4, 1999.

Wexler, A. S., and Clegg, S. L.: Atmospheric aerosol models for systems including the ions H^+, NH_4^+, Na^+, SO_4^{2-}, NO_3^-, Cl^-, Br^-, and H_2O, J. Geophys. Res. Atmos., 107, ACH 14-11-ACH 14-14, https://doi.org/10.1029/2001JD000451, 2002.

Whalley, L. K., Furneaux, K. L., Goddard, A., Lee, J. D., Mahajan, A., Oetjen, H., Read, K. A., Kaaden, N., Carpenter, L. J., Lewis, A. C., Plane, J. M. C., Saltzman, E. S., Wiedensohler, A., and Heard, D. E.: The chemistry of OH and HO_2 radicals in the boundary layer over the tropical Atlantic Ocean, Atmos. Chem. Phys., 10, 1555-1576, https://doi.org/10.5194/acp-10-1555-2010, 2010.

Whalley, L. K., Stone, D., Dunmore, R., Hamilton, J., Hopkins, J. R., Lee, J. D., Lewis, A. C., Williams, P., Kleffmann, J., Laufs, S., Woodward-Massey, R., and Heard, D. E.: Understanding in situ ozone production in the summertime through radical observations and modelling studies during the Clean air for London project (ClearfLo), Atmos. Chem. Phys., 18, 2547-2571, https://doi.org/10.5194/acp-18-2547-2018, 2018.

Whalley, L. K., Slater, E. J., Woodward-Massey, R., Ye, C., Lee, J. D., Squires, F., Hopkins, J. R., Dunmore, R. E., Shaw, M., Hamilton, J. F., Lewis, A. C., Mehra, A., Worrall, S. D., Bacak, A., Bannan, T. J., Coe, H., Ouyang, B., Jones, R. L., Crilley, L. R., Kramer, L. J., Bloss, W. J., Vu, T., Kotthaus, S., Grimmond, S., Sun, Y., Xu, W., Yue, S., Ren, L., Acton, W. J. F., Hewitt, C. N., Wang, X., Fu, P., and Heard, D. E.: Evaluating the sensitivity of radical chemistry and ozone formation to ambient VOCs and NOx in Beijing, Atmos. Chem. Phys. Discuss., 2020, 1-41, https:\\doi.org\10.5194/acp-2020-785, 2020.

Winer, A. M., and Biermann, H. W.: Long pathlength differential optical absorption spectroscopy (DOAS) measurements of gaseous HONO, NO_2 and HCNO in the California South Coast Air Basin, Res. Chem. Intermed., 20, 423-445, https://doi.org/10.1163/156856794X00405, 1994.

Wu, L., Li, X., and Ro, C.: Hygroscopic behavior of ammonium sulfate, ammonium nitrate, and their mixture particles, Asian J. Atmos. Environ., 13.3, 196-211, https://doi.org/10.5572/ajae.2019.13.3.196, 2019.

Ye, C., Zhou, X., Pu, D., Stutz, J., Festa, J., Spolaor, M., Tsai, C., Cantrell, C., Mauldin, R. L., Campos, T., Weinheimer, A., Hornbrook, R. S., Apel, E. C., Guenther, A., Kaser, L., Yuan, B., Karl, T., Haggerty, J., Hall, S., Ullmann, K., Smith, J. N., Ortega, J., and Knote, C.: Rapid cycling of reactive nitrogen in the marine boundary layer, Nature, 532, 489-491, https://doi.org/10.1038/nature17195, 2016.

Ye, C., Heard, D. E., and Whalley, L. K.: Evaluation of novel routes for NO_x formation in remote regions. , Environmental Science Technology, 51, 7442-7449, https://doi.org/acs.est.6b06441, 2017a.

Ye, C., Zhang, N., Gao, H., and Zhou, X.: Photolysis of particulate nitrate as a source of HONO and NO_x, Environ. Sci. Technol., 51, 6849-6856, https://doi.org/10.1021/acs.est.7b00387, 2017b.

Zhou, X., Gao, H., He, Y., Huang, G., Bertman, S. B., Civerolo, K., and Schwab, J.: Nitric acid photolysis on surfaces in low NO_x environments: Significant atmospheric implications, Geophys. Res. Lett., 30, 2217, https://doi.org/10.1029/2003GL018620, 2003.